Examining the symmetry of optical flares in blazars

Master's Thesis
University of Turku
Dept. of Physics and Astronomy
Astronomy
2019
BSc Jenni Jormanainen
Reviewed by:
Prof. Juri Poutanen
Dr. Talvikki Hovatta

The originality of this thesis has been checked in accordance with the University of Turku quality assurance system using Turnitin OriginalityCheck service.

UNIVERSITY OF TURKU
Department of Physics and Astronomy
JORMANAINEN, JENNI Examining the symmetry of optical flares in blazars
Master's Thesis, 55 pages
Astronomy
October 2018

Blazars are one of the most energetic types of active galactic nuclei. They are luminous emitters that can be detected over the whole of the electromagnetic spectrum. They are radio-loud objects whose jet is closely aligned to our line of sight, which together with the relativistic jet speeds cause Doppler boosting to the jet. Because of the Doppler boosting, blazars are extremely variable objects and their luminosities have been detected to vary on time scales of years to days and all the way down to minutes. They possess strong radio and optical polarization that is also known to vary. Blazars can be divided into two main classes of BL Lacertae objects (BL Lacs) and flat-spectrum radio quasars (FSRQs) based on their spectral properties.

In this thesis I studied the symmetry of the optical flares in long-term blazar light curves obtained within the Tuorla Blazar Monitoring Program. In the analysis, I utilized a Bayesian blocks method, which decomposes the light curves into individual flaring episodes. The symmetry and its correlation with other obtained parameters were examined and compared between the different blazar types.

The flares were found to be mostly symmetric, which is in accordance with other studies made on the subject. This implies that the variability in the optical band is tied to the light crossing time across the emission region. This study showed that the symmetric or asymmetric behaviour of the flares is similar in different types of blazars. Investigating the symmetry of the flares further in the optical band can give a means to constrain the region of the optical emission, clues for the composition of the jet, and shed light on the mechanisms that accelerate particles in the jet.

Keywords: active galactic nuclei, blazar, BL Lacertae object, flat spectrum radio quasar, light curve, optical flares, symmetry

Contents

1 Introduction

Active galactic nuclei (AGN) are galaxies that are powered by actively accreting supermassive black holes (SMBH) in their nucleus. These central engines are known to have masses higher than 10^6 $M_\odot$ [1, 2]. AGN are among the most luminous and energetic phenomena in the universe that are detectable to high redshifts. They can be distinguished from normal galaxies in different ways such as the high luminosity, broad-band continuum emission, strong emission lines, small angular size, flux variability on time scales of years to months and even minutes [3–9], or, for a minority of the AGN, relativistic jets shot out from the poles of the central engine. Despite there being a number of ways to distinguish an AGN from a normal galaxy, not all AGN possess all the features that can define an active galaxy. It is known that all galaxies host a supermassive black hole in their centre but the division into active and non-active galaxies is not entirely clear as there are varying stages of activity. This has lead to a vast "zoo" of active galactic nuclei with several different categories to classify and identify these objects [10].

The general picture of the structure of an AGN is depicted in Figure 1, which shows the zoomed-in view of the galactic nucleus. In the center is the supermassive black hole, surrounded by an accretion disk of hot gas and dust. Around the nucleus is an obscuring, dusty torus, which blocks the view to the nucleus of AGN that are viewed edge-on. Closer to the central engine is the broad line region (BLR) and further away the narrow line region (NLR). This figure shows the radio-loud case where radio jets are launched from the vicinity of the poles of the SMBH. In the radio-quiet case these jets are not seen. It is also debated that there would exist a hot corona around the core producing the hard X-ray continuum often detected in AGN. According to the unification of active galactic nuclei, the different features that are observed in different types of AGN depend both on their alignment, but the observed differences can also be due to their intrinsic properties. [11, 12]

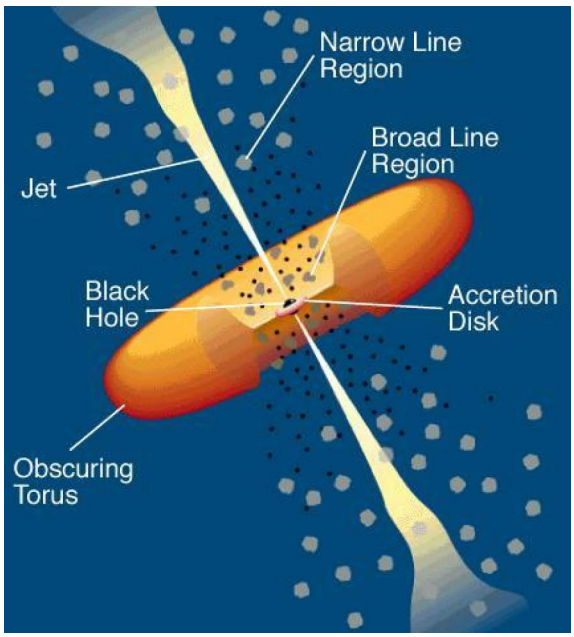

Figure 1. Model of a radio loud AGN showing the central black hole, the surrounding accretion disk, broad and narrow line regions, the dusty torus, and the radio jets launched from the vicinity of the SMBH. [13]

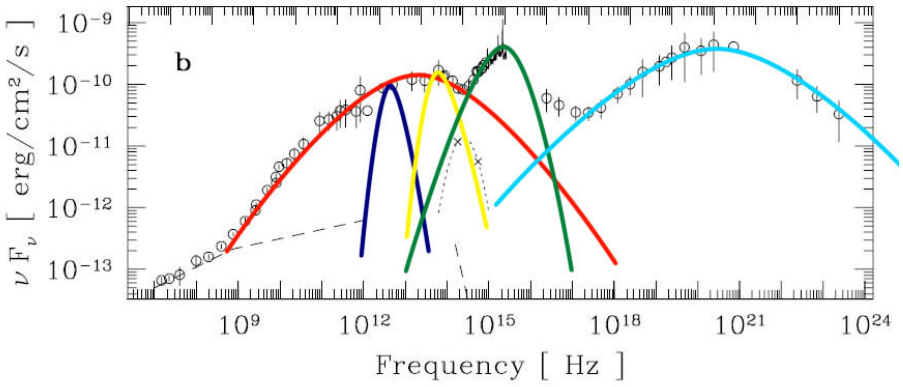

Figure 2. Spectral energy distribution of 3C 273 [14] with the different emission components visualized with parabolas; synchrotron radiation from the jet in red, inverse-Compton radiation from the jet in light blue, blackbody radiation from the accretion disk in green, blackbody radiation from the host galaxy in yellow, and blackbody radiation from heated dust in dark blue.

1.1 Broad-band emission

When comparing the spectral energy distributions (SEDs) that are observed from AGN to the SEDs of normal galaxies, the frequencies in which the AGN can be detected span all the way from radio emission to the High Energies (HE) and Very High Energies (VHE) in gamma-rays. Figure 2 shows the different emission components that can be visible in different types of galaxies. The SED of normal galaxies consists almost only of the thermal spectrum radiated by the stars but there can also be some contribution by dust that reradiates the starlight in the far-infrared region. In AGN, however, the different parts of the nucleus produce emission by thermal and non-thermal processes. Based on whether or not synchrotron emission in radio frequencies is seen in the spectrum, the AGN can be divided into radio-loud and radio-quiet objects [15, 16]. As in normal galaxies, also in AGN the host galaxy contributes to the thermal emission of the spectrum, but unlike in normal galaxies, in AGN the accretion disk and the dusty torus also produce thermal emission. This can be seen in all the way through far-infrared to optical to UV. The X-ray spectrum is known to be produced near the central engine and is thought to originate from the upscattered UV emission of the accretion disk in the hot corona. In the case of radio-loud AGN the X-ray emission can also be produced through inverse-Compton (IC) mechanisms by nonthermal synchrotron electrons. The highest energy emission seen in the gamma-rays is again produced in the jets through IC mechanisms although the details, whether the jet consists of hadrons or leptons, are still under a debate. [17]

1.2 Blazars

One of the most energetic AGN types are blazars. They are luminous emitters and can be detected over the whole broad band of the electromagnetic spectrum, some even all the way up to gamma-rays. Their key characteristic is a powerful jet closely

aligned to our line of sight [11], which together with the relativistic jet speeds causes Doppler boosting to the radiation produced by the jet that is seen in the front and deboosting to the jet moving away from us. They are radio-loud objects with high variability and strong radio and optical polarization [18].

Blazars can be divided into two main classes of BL Lacertae objects (BL Lacs) and flat-spectrum radio quasars (FSRQs). Whereas BL Lacs have mostly nonexistent or very weak emission lines, which can be due to the flaring jet overshadowing the emission from the other parts of the galaxy or the spectral lines can be intrinsically weak, FSRQs possess luminous broad emission lines [19].

The division between these two classes is thought to be due to different parent populations. The Fanaroff-Riley type I (FR I) [20] is thought to be the misaligned parent population of BL Lacs, and the FR II the misaligned counterpart for the FSRQs but this has been observed to not always being true [21, 22]. In addition, BL Lacs are usually divided further into high peaking BL Lacs (HBL), intermediate peaking BL Lacs (IBL), and low peaking BL Lacs (LBL) based on the peak frequency of their synchrotron emission component in their SEDs [23]. Because of their varying nature, these classes experience some fluctuations due to the flaring or non-flaring states of their central engines, and therefore the classification of these objects is not always unambiguous. For example in the case of the namesake of the BL Lacertae objects, BL Lac was first classified as a BL Lac or an HBL when it was in its flaring state but later showed some signs of emission lines and was later reclassified as an LBL. [11, 24–28]

The detection of the blazar host galaxies can offer important clues about their underlying parent populations. BL Lacs have been observed to typically reside in massive elliptical galaxies that are similar to normal nonactive elliptical galaxies [29]. FSRQs reside in more luminous ellipticals than BL Lacs referring that these two types of objects indeed belong to a common class of AGN [30].

1.3 Jets

In radio-loud AGN, there are collimated outflows, or jets, that are being launched near the poles of the central supermassive black hole. They can carry out energy, momentum and angular momentum over great distances from the center. Their composition and how they are being generated or what keeps them collimated are still uncertain but according to the theoretical models they are most likely launched due to the magnetic field extracting energy from the black hole or the accretion disk. Generally, the jet structure in AGN is divided into the large-scale jet extending over several kiloparsecs, and smaller, parsec-scale jets.

1.3.1 Large-scale jets

Radio galaxies are traditionally divided into two classes based on the structure and luminosity of their large-scale jets. In the case of FR I radio galaxies, the jets themselves are prominent, usually asymmetric, ending in plumes, and are two-sided. In FR II type of galaxies the jets themselves are weak, often one-sided, and they end in radio lobes with bright hotspots that, however, are seen on both sides. Why the jets in FR I and FR II galaxies differ from each other; whether they are intrinsically different [31] or if they differ due to environmental effects [32, 33], is not known exactly. The correlation of the large-scale jet with the parsec-scale jet would imply that the jets would originate as the consequence of bulk relativistic outflows from the AGN. [20]

The large-scale jets can be seen over the whole broad-band spectrum. Radio to optical emission of the jets is thought to be due to synchrotron radiation, but it is known for sure only for FR I AGN that also the X-ray emission is due to synchrotron radiation. [34–36]. Higher energy X-ray emission could be either due to the IC mechanisms, in which case the jet would essentially consist of leptons (leptonic model) and would follow from the scattering of low-energy photons from the jet as

in synchrotron self-Compton process (SSC) [37–39], or of photons of external origin (external Compton process, EC) [40, 41]. Another possibility of producing high-energy synchrotron radiation is described by the hadronic model where the non-thermal radiation is caused by ultrarelativistic protons and their secondary particle cascades. [42–44].

1.3.2 Parsec-scale jets

Compared to the large-scale jets that are known to be two-sided due to the symmetric large radio structures, the pc-scale jets often appear one-sided. The reason to this lies in the relativistic beaming, or Doppler boosting, that is a consequence of the jet geometry and relativistic speeds observed in AGN jets; while the jet pointing closer to the direction of our line of sight is boosted to appear brighter, the jet moving away from us is de-boosted beyond the limits of observations. Since the pc-scale jets extend only a few parsecs away from the core, Very Long Baseline Interferometry (VLBI) is needed to observe their structure due to better angular resolutions. [45,46]

In blazars, the jets are observed within a small angle ($\theta \lesssim 10$ °) along our line of sight [47]. Due to the Doppler boosting, the velocities in blazars appear to surpass the speed of light with observed velocities even up to $50c$ [48]. As the brightness also experiences the effects of boosting, the brightness variations in blazars are further exaggerated. These variations are believed to be caused when a perturbation in the jet, a "blob" or a "knot", emerges near its base. The apparent velocities β_{app} of these blobs can be measured using VLBI observations by detecting the distance the blob has moved in a certain time when the redshift of the source is known. [48, 49]

1.4 Acceleration mechanisms in jets

The essential attributes in studying jets are the acceleration mechanism of the particles and the composition of the jet. There are several acceleration mechanisms

available to explain the flaring in the jets but only a few of them can be considered to explain the spectral energy distribution, variability, and the strong polarization seen in blazars. In this Section, a few of the most relevant acceleration mechanisms are considered.

1.4.1 Shock model

The shock model is commonly thought to have an important role in describing the acceleration of the particles in the jets [50–54]. The shock model in general is rather well-known, and it is able to recreate the observed power-law non-thermal particle spectrum that is seen in blazar SEDs [55].

A shock is usually defined as a part of the jet where the speed of the flow drops from supersonic upstream speed to the subsonic downstream speed. The way the shocks transport energy to particles is commonly thought to happen through the first-order Fermi acceleration. In this mechanism, a particle will gain energy through crossing the shock front. When the particle crosses the front of the shock it will be scattered off of the irregularities within the plasma flow and will gain energy. The energies seen in blazar jets are extremely high so therefore the shock crossing must somehow be able to accelerate the particles to high energies before they escape the shock. In order to escape, a particle must cross the shock upstream. However, because the velocities in the relativistic shocks are close to the speed of light, the particles are less likely to cross the shock upstream but rather are caught up with the shock and forced to cross back downstream. When the particles cross the shock fronts repeatedly, the energies they gain can reach all the way up to the TeV range. [56, 57]

In reality, the relativistic case of the first-order Fermi acceleration needs further corrections and it has been thought to work through the particles crossing Alfvén waves frozen-in to the plasma. Because the shock model is not easy to apply to the

real case of the blazar jets, and because some of the shock model simulations do not produce the high optical polarization observed in blazars, also other mechanisms should be considered to be acting on the jet. [55, 57]

1.4.2 Stochastic acceleration

Another way for the particles to accelerate in blazar jets is thought to be through stochastic acceleration, or second-order Fermi acceleration, by turbulence, which is also able to produce the power-law spectra seen in blazars. In the cases where the first-order mechanism does not fully explain the observed spectra, stochastic acceleration could be used to improve the first-order spectrum. The shock acceleration requires that there exists some scattering agent, generally thought to be plasma turbulence, that will force the particles to cross the shock front. The way stochastic acceleration works is through resonant interactions of the particles caused also by the turbulence, and it is able to complement or even replace the shock model when flatter spectra are needed. [58]

Based on polarization-dependent radiation simulations, the shock model causes the polarization degrees (PD) above 40% -50%, and therefore it cannot be the only model to explain the PDs of 10% -20% [59] typically observed in blazars but turbulence is needed to lower the PD. Although stochastic model or some other turbulent model could be able to explain the SED commonly seen in blazars, these mechanisms needs shocks to create turbulence in the jet, they would likely be a complimentary acceleration mechanism together with the shock model. However, stochastic acceleration does not reproduce the deterministic polarization angle (PA) swings and it seems to be more likely that it would only be part of the solution for the acceleration that takes place in the blazar jets. [55]

1.4.3 Magnetic reconnection

A third possible explanation for the flaring activity is a more recent theory of kink instabilities causing magnetic reconnection to accelerate the particles in the jets [60]. Magnetic reconnection has generally been accepted to be the main mechanism of particle acceleration in the Sun, but has only recently been studied more widely in AGN jets. Recent studies show that magnetic reconnection could be able to account for the high PD and the PA swings seen in jets as well as for the reproduction of the typical blazar SED [55].

In magnetic reconnection, the magnetic energy from the jet emission region is released and converted into heating of the plasma and acceleration of the particles when two field lines of opposite polarity get close to each other and annihilate due to the instabilities in their environment. In magnetically dominated plasmas, reconnection can be an efficient way to accelerate particles and it is thought to work through leptons. [55,61]

There have also been simulations that show the magnetic field evolving in the jet while the jet can still remain collimated [55,62,63], and new models that use the magnetic reconnection to explain the flares that cause the multi-timescale variability seen in blazars [64,65].

1.5 Optical emission in blazars

Optical emission in blazars has been studied ever since the discovery of this peculiar extragalactic class of objects, first by observing the irregular variability of BL Lacertae, first thought to be a star, and later recognized to possess similarities to quasars [66,67]. Due to Doppler boosting, the jet emission dominates in blazar spectral energy distributions and the optical emission is located in the flat part of the synchrotron component. In BL Lacs, most of the optical emission observed originates from the synchrotron emission of the jet but the host galaxy contribution

can also be seen in the higher synchrotron peak BL Lacs due to their low redshifts, and in lower synchrotron peaking objects during their non-flaring state when the jet emission is not as strong. In FSRQs, their SEDs also show the UV bump from the accretion disk, and their spectra show broad emission lines produced in the BLR. In both cases, however, the host galaxy is often very difficult to detect behind the bright jet though it is often seen as a nebular structure surrounding the bright core, and in lower peaking BL Lacs and FSRQs the host galaxy emission lines can be seen although they are often weaker than in other AGN. [11, 68]

Blazars are highly variable (fluctuations of few magnitudes) also in the optical wavelengths. In most blazars, optical variability shows no signs of periodicity and it is detected on time scales of days to years and even hours. Multi-wavelength variability studies can be used to constrain the size of the emission region, jet geometry, and acceleration mechanisms acting on the jet. For example, the optical-IR emission and the gamma-ray emission have been found to correlate, which would support the leptonic model that the optical and gamma-ray emission are due to the same population of electrons. [68, 69]

As well as being highly variable, blazars are highly optically polarized [70]. Optical emission can be used to observe the central nuclear regions of blazars where the radio emission would normally be self-absorbed. Polarization studies can also be used in studying the magnetic fields in the jets. [68]

1.5.1 Symmetry of optical flares

While there have been several studies of the optical variability of blazars (e.g. [3, 69, 71–73]), symmetry of the blazar flares in the optical band has not been studied extensively (e.g. [69, 73]). While the division of the light curves into flares might not describe the jet events in reality, this thesis focuses only on the largest changes of flux density instead of going down to the smallest time scales where it may not

be feasible to call these events "flares". However, the models used for the biggest changes in flux density over longer time scales seem to produce shapes that resemble flares, in addition to which the radio observations of the pc-scale jets clearly show separate radio blobs emerging from the jet that could also be described as flares. The brightest flares seen in optical usually have a connection with these radio blobs. The previous studies that have utilized similar models as was used in this thesis have also been able to use the fitted information to estimate the size of the emission region, which indicates that the models, although unphysical, manage to explain some aspects of the nature of the jets. Investigating the symmetry in the optical band can give a means to constrain the region of the optical emission [73], clues for the composition of the jet [69], and shed light on the mechanisms that accelerate particles in the jet [55].

In this thesis, symmetry of flares in long-term light curves of 31 blazars is studied. This is the first systematic study of the flare symmetry in a large sample of objects. The rest of the thesis is constructed so that in Section 2 the data and the used data analysis methods are briefly explained. In Section 3, the results of the data analysis are shown. In Section 4, interpretations of the results and comparisons to other similar studies are made. Finally in Section 5, conclusions are drawn.

2 Data and the methods

2.1 Observations and data acquisition

The data used in this thesis are from the Tuorla Blazar Monitoring Program[1] [74] that was initiated in 2002 as the optical counterpart for the VHE gamma-ray observations by the MAGIC Telescopes. The sample consists of 31 blazars visible from the Northern hemisphere observed in the optical R-band between 2002-2012. All

[1] http://users.utu.fi/kani/1m/

the blazars used here have also been detected in the TeV range or are possible TeV candidates. [71]

The observations for this program were first done with the Tuorla Observatory 1.03-meter telescope located in Piikkiö, Finland but starting from 2004 the 35-cm Celestron attached to the main telescope of the KVA (Kunliga Vetenskapsakademien) observatory located at the island of La Palma, Spain, has been used as the main telescope of the program. The data have been acquired using three different CCD cameras and the R-band filter. For the data reduction, the bias and dark images were taken each night and the flat-field images every month. The data were reduced and the magnitudes measured with a semi-automatic Diffphot pipeline made by Kari Nilsson [75]. In the reduction, the combined dark and bias images were subtracted from the science frames, which were then divided by the flat-field image. The flux densities of the target and the control and comparison stars were measured using differential photometry, and the true magnitudes calculated based on the calibration flux densities. The more detailed description of the data and the data reduction are given in [71].

The sources used in this thesis are listed in Table 1. The sample includes all the different types of blazars but the majority consists of the high peaking BL Lacs. All in all there are 22 HBLs, three clear IBLs and two sources that were classified as either IBLs or HBLs but in this thesis were treated as IBLs, two LBLs, and two FSRQs [71]. HBLs dominate the sample due to the original selection criteria of the TeV BL Lac candidates that the objects are bright both in radio band and in X-rays [76]. This is prone to cause some bias in the analyses and must be taken into account. The table also lists the coordinate information of the sources, the redshifts if determined, and the synchrotron frequency peaks for all the sources as listed in [71]. The luminosity distances were calculated using the Cosmology Calculator[2] [77]. The variability Doppler factors and the Lorentz factors were derived from the data

[2]http://www.astro.ucla.edu/ wright/CosmoCalc.html

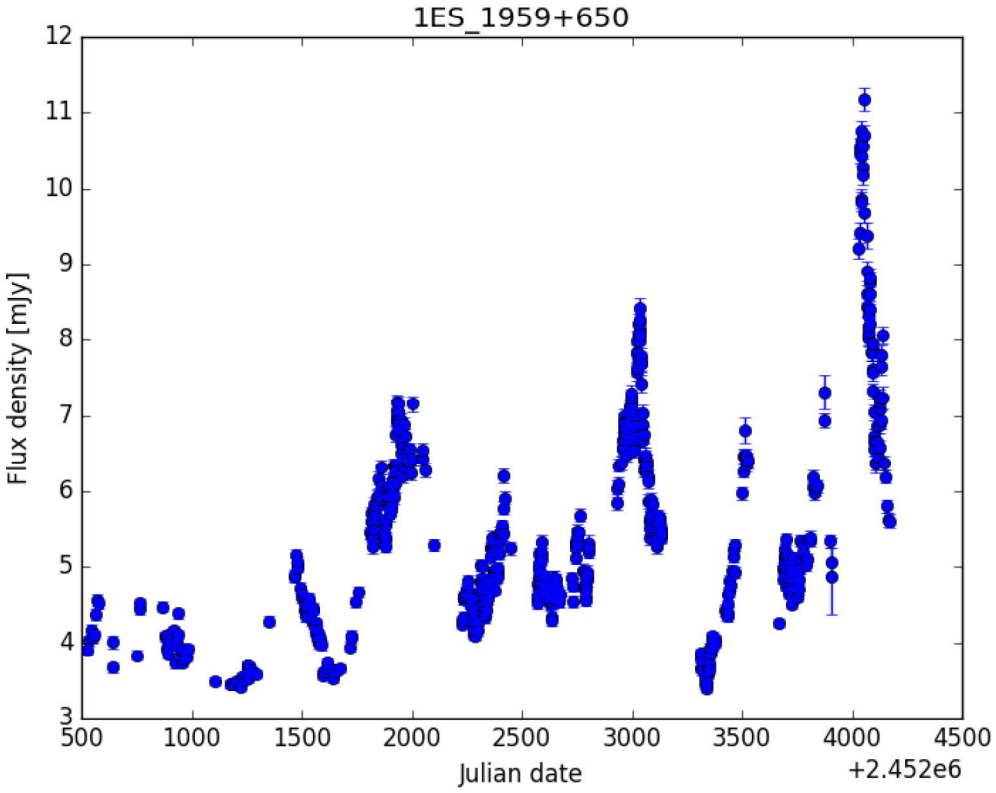

Figure 3. The lightcurve of 1ES 1959+650 shows an example of a well-sampled dataset with small errorbars in terms of flux density and only having the seasonal gaps in observations. The observations for this light curve have been done between 13/08/2002 and 26/07/2013.

taken with the Owens Valley Radio Observatory 40-metre Telescope at 15 GHz [78].

Because in optical observations each source has about a 180-200 day season when they are unobservable during the night, all the light curves have these seasonal gaps. In order to avoid making false assumptions on the continuity of the light curve during the gaps, the data were divided into seasons, and each season was then treated separately. The criterion of the division of one season was an equal to or longer gap than a 100 days. Figures 3 and 4 show examples of the light curves used in this thesis. In Figure 3 the light curve of 1ES 1959+650, a bright high declination source, is well-sampled with few gaps during each observational season and very small error bars in terms of the flux density. Most flares also have slow rise and decay times. In contrast, the light curve of RGB 1417+257, a much fainter lower declination source in Figure 4, has larger errorbars and rapid changes of smaller magnitude making the separation of each individual flare more difficult even by eye.

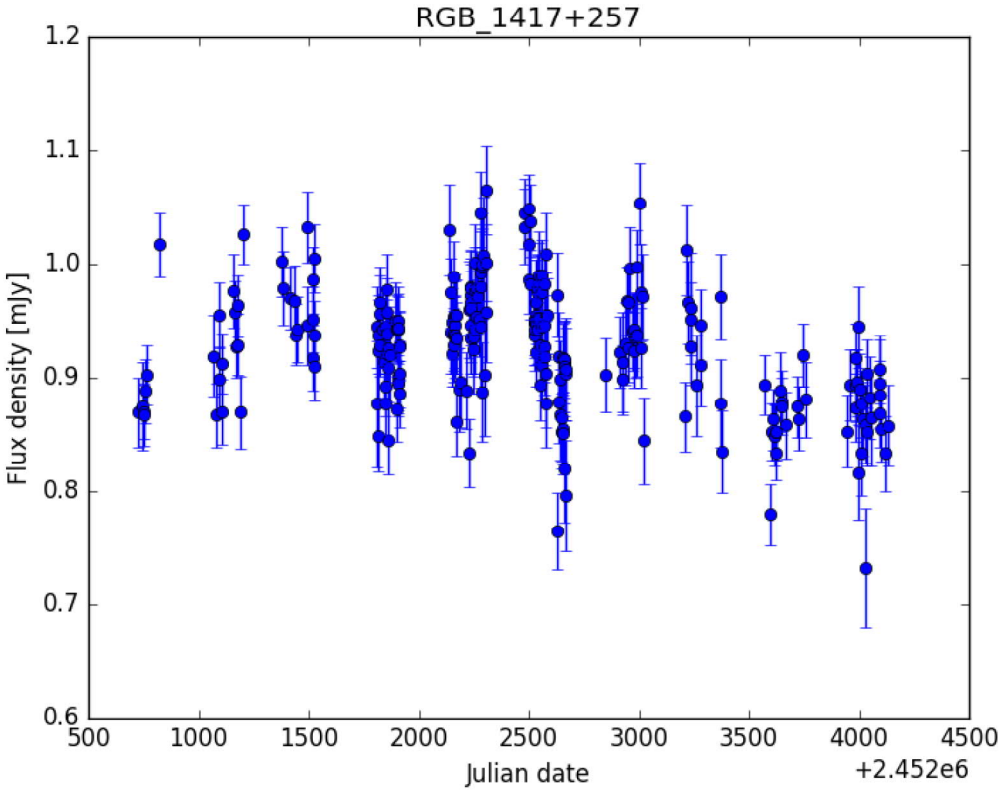

Figure 4. The lightcurve of RGB 1417+257 shows how in fainter sources the error bars are larger, and there exists fast but not very distinctive variations of the flux density in between the seasonal gaps. The observations for this light curve have been done between 13/08/2002 and 26/07/2013.

Table 1. Each source with their coordinates, blazar type, redshifts if defined [71], calculated luminosity distances based on redshift [77], synchrotron frequency peaks [71], variability Doppler factors, and Lorentz factors [78]

Target	RA	DEC	Type	z	d_L [Mpc]	$\log(\nu_{peak}[\mathrm{Hz}])$	D_{var}	Γ
1ES 0033+595	00 35 52.6	+59 50 05	HBL	-	-	18.17±0.14	-	-
1ES 0120+340	01 23 08.8	+34 20 50	HBL	0.272	1400	17.66±0.13	-	-
RGB 0136+391	01 36 32.7	+39 06 00	HBL	-	-	16.00±0.30	-	-
RGB 0214+517	02 14 17.9	+51 44 52	HBL	0.049	219	16.08±0.07	-	-
3C 66A	02 22 39.6	+43 02 08	IBL	0.444	2480	14.15±0.09	3.40	-
1ES 0647+250	06 50 46.5	+25 03 00	HBL	0.41	2260	16.41±0.23	-	-
1ES 0806+524	08 09 49.2	+52 18 58	HBL	0.138	656	15.84±0.14	-	-
OJ 287	08 54 48.9	+20 06 31	LBL	0.306	1600	13.27±0.07	29.8	18.75
1ES 1011+496	10 15 04.2	+49 26 01	HBL	0.212	1050	15.63±0.26	0.458	6.22
1ES 1028+511	10 31 18.5	+50 53 36	HBL	0.36	1940	16.70±0.26	-	-
Mkn 421	11 04 27.3	+28 12 32	HBL	0.031	137	17.03±0.19	-	-
RGB 1117+202	11 17 06.2	+20 14 08	HBL	0.139	661	15.98±0.12	-	-
Mkn 180	11 36 26.4	+70 09 27	HBL	0.045	201	16.47±0.25	1.06	-
RGB 1136+676	11 36 30.1	+67 37 04	HBL	0.135	640	17.90±0.29	-	-
ON 325	12 17 52.1	+30 07 01	IBL/HBL	0.13	615	14.85±0.18	3.04	1.69
1ES 1218+304	12 21 21.9	+30 10 37	HBL	0.182	889	17.17±0.23	-	-
RGB 1417+257	14 17 56.6	+25 43 25	HBL	0.237	1200	17.62±0.10	-	-
1ES 1426+428	14 28 32.6	+42 40 21	HBL	0.129	610	18.02±0.26	-	-
1ES 1544+820	15 40 15.7	+81 55 06	HBL	-	-	16.04±0.21	-	-
Mkn 501	16 53 52.2	+39 45 37	HBL	0.034	150	16.47±0.06	0.230	3.97
OT 546	17 28 18.6	+50 13 10	HBL	0.055	247	16.35±0.20	0.214	-
1ES 1959+650	19 59 59.8	+65 08 55	HBL	0.047	210	16.70±0.04	1.60	-
BL Lac	22 02 43.3	+42 16 40	LBL	0.069	313	13.99±0.12	12.2	10.2
1ES 2344+514	23 47 04.8	+51 42 18	HBL	0.044	196	16.35±0.12	1.33	1.04
S5 0716+714	07 21 53.4	+71 20 36	IBL	0.31	1630	14.24±0.13	31.3	21.22
ON 231	12 21 31.7	+28 13 59	IBL	0.102	473	14.32±0.08	2.67	17.09
3C 279	12 56 11.1	−05 47 22	FSRQ	0.536	3110	12.69±0.05	11.6	24.06
PG 1424+240	14 27 00.4	+23 48 00	IBL/HBL	0.604	3500	15.14±0.07	-	3.21
PKS 1510−089	15 12 50.5	−09 06 00	FSRQ	0.36	1940	13.75±0.15	32.1	28.37
PG 1553+113	15 55 43.0	+11 11 24	HBL	-	-	15.90±0.16	-	-
PKS 2155−304	21 58 52.0	−30 13 32	HBL	0.116	543	16.01±0.28	-	-

2.2 Methods

In order to examine the symmetry of the flares in blazars, a method to separate individual flares from the light curves is needed. In this thesis, a method of exponential fitting was attempted first since it had proven to be a useful way of investigating the light curves using the flux density variations and has been done successfully before in radio [79, 80], optical, and gamma-rays [3, 69, 73]. Since the long-term observational data from the Tuorla Blazar Monitoring Program proved to be too poorly sampled for the exponential decomposition, the Bayesian blocks method [81,82] was implemented and proved to work better for these data. In the following sections the two methods are described briefly, and their pros, cons and possible future uses are discussed.

2.2.1 Exponential fitting

Exponential fitting, first introduced by [79], is an unphysical tool used to fit exponential flares in the flux density light curves of blazars. The idea behind this method is to determine the rise and decay times of individual flares in the light curves by fitting the increases and decreases of the flux density with exponential curves. In radio, this allows the determination of the variability time scale, which is assumed to relate to the light travel time across the emission region, and can be used to estimate its size [79]. The fitted exponentials have a form

$$\Delta S(t) = \begin{cases} \Delta S_o(\nu) e^{(t-t_{max})/\tau_r}, t < t_{max}, \\ \Delta S_o(\nu) e^{(t_{max}-t)/\tau_d}, t > t_{max}. \end{cases} \quad (1)$$

Here $\Delta S_o(\nu)$ is the amplitude of the flare in Jy, t_{max} is the epoch of the flare maximum, τ_r is the rise time, and τ_d is the decay time of the flare in days [80]. The final model is then the superposition of these shapes.

The variability Doppler factor can be calculated from the decomposition by first solving the brightness temperature from the Rayleigh-Jeans law

$$I(\nu) = \frac{2\nu^2 k_B T_{b,var}}{c^2}, \tag{2}$$

where, ν is the observing frequency, $I(\nu)$ is the observed intensity, and it is given by $I_\nu = \Delta S_o(\nu)/\Delta\Omega$. Here $\Delta\Omega$ is the solid angle that is given by $\Delta\Omega = \frac{\pi R^2}{d_L^2}(1+z)^2$, where d_L is the luminosity distance and z is the redshift. The emission region size is given by $R = c\tau_r D_{var}$, where D_{var} is the Doppler factor. Additional redshift transformation is needed for frequency, and we obtain

$$T_{b,var} = 1.47 \cdot 10^{13} \frac{d_L^2 \Delta S_o(\nu)}{\nu^2 \tau_r^2 (1+z)^4} \text{ K}, \tag{3}$$

where d_L is in Mpc, ν is in GHz [78]. From the brightness temperature, the variability Doppler factor can be calculated in the following way

$$D_{var} = \left[\frac{T_{b,var}}{T_{b,int}}\right]^{1/3}, \tag{4}$$

where $T_{b,int}$ is the intrinsic brightness temperature of the source. The value of $T_{b,int}$ has been under debate but it is often assumed to be the equipartition temperature, approximately 10^{11} K. [79, 80, 83, 84]

Velocity of the jet is given by $\beta = v/c$, where v is the measured jet speed. When the jet is viewed at a small angle θ, the apparent velocity is given by

$$\beta_{app} = \frac{\beta \sin\theta}{1 - \beta\cos\theta}. \tag{5}$$

This results in Doppler beaming of the emission, by the Doppler boosting factor

$$D = \frac{1}{\Gamma(1 - \beta\cos\theta)}, \tag{6}$$

where $\Gamma_{var} = (1-\beta^2)^{-1/2}$ is the bulk Lorentz factor. When the Doppler factors have been determined from Equation 4 and the apparent velocities have been measured, the jet bulk Lorentz factor and the viewing angle can be solved using Equations 5 and 6 [85]

$$\Gamma_{var} = \frac{\beta_{app}^2 + D_{var}^2 + 1}{2D_{var}} \tag{7}$$

$$\theta_{var} = \arctan\left(\frac{2\beta_{app}}{\beta_{app}^2 + D_{var}^2 - 1}\right). \tag{8}$$

Previous works [79, 80, 86] have shown that with a simple model like this it is possible to acquire essential information about the jet physics and that the modelled flares describe the jet properties well in reality.

In order to analyse the optical light curves in this thesis, a Markov Chain Monte Carlo (MCMC) modelling procedure Magnetron2 written by Daniela Huppenkothen was attempted [87]. The method utilizes MCMC in the form of Diffusive Nested Sampling as in DNest [88]. Originally, Magnetron2 was developed for fitting magnetar light curves in X-rays. In [87], the magnetar light curves are called bursts and each burst is divided into components, which are the fitted exponential curves. The produced posterior distribution samples can then be studied to uncover the

properties of individual burst components.

Because the code utilizes iterative nature of Bayesian methods, the poor sampling of the optical light curves lead to non-convergence and either bad fits or infinite runtime in most cases. The tweakable priors in the model are the minimum and maximum component amplitude, and the minimum and maximum number of flares. In the optical case, the maximum of 0.1 Jy for the amplitude was used. Further along the experimenting also other values were tested. Division of the data into seasons was attempted in order to make up for the gaps in the data. After prolonged attempts to make the code work for the data at hand, the code was deemed unsuitable for the needs of this thesis. Magnetron2 was able to produce good fits only for the full light curve of 1ES 1959+650 but when cut into seasons the code was unable to create a good fit even for such a well-sampled source. With the rest of the sources, neither full light curves nor the seasonal parts could be fitted. Also, an exponential fitting code written by Ritaban Chatterjee [3] was tested but the same problems occurred as with Magnetron2.

With futher studies, Magnetron2 might prove to be a good way to fit the exponentials and also their errors, but in the short time frame of this thesis it was impossible to make it work for these data. In the future and with better sampled data, Magnetron2 should be considered as a powerful option for fitting the light curves also in the optical range. In radio, Magnetron2 has been successfully used for data observed with the Owens Valley Radio Observatory (OVRO) 40-m Telescope to produce the variability Doppler factors and the bulk Lorentz factors used in this thesis. The apparent jet speeds β_{app} used by [78] to calculate the bulk Lorentz factors were determined from 15 GHz VLBA data in the Monitoring Of Jets in Active galactic nuclei by VLBA Experiments (MOJAVE) program [48].

2.2.2 Bayesian blocks

The method that was used in fitting the light curves in this thesis was the Bayesian blocks method first introduced by Jeffrey D. Scargle. The method is one possible solution to the problem of recognizing structures in photon counting data. Since the procedure does not have a lower limit on the time scale of the variability detection, it is suitable for analysing blazars, in which the variability time scale varies from minutes to months and years. The Bayesian blocks method aims to separate statistically significant changes in the data from the the observational errors without assumptions about the smoothness or the shape of the signal. The algorithm also aims to handle data that are not gapless or evenly spaced, therefore being able to decompose the optical light curves when divided into seasonal gaps. [81, 82]

The code used here was written by Yannis Liodakis and it uses a hill-climbing algorithm together with the Bayesian blocks method to separate the individual flares. The Bayesian blocks method divides the light curves based on changes in the flux density. The hill-climbing part of the code simply recognizes the turning point, in which the slope of the flux density in one block changes sign signifying the decay of a flare. This is also a weakness of this method as it does not recognize overlapping flares, but as is noticed later in Section 4.1, using the Bayesian blocks gives similar results as the exponential method, which does detect flares that overlap. Despite the Bayesian blocks method not needing a smoothed or interpolated data, the code used here smooths the data by a three-day median in order to detect the underlying trends more easily. The code has only one tweakable prior, *gamma*, which is the prior for the number of blocks in the light curve and it can have values between $[10^{-\infty}, 1]$. With values closer to 1 more flares were fitted and vice versa with values close to 0. The suitable value of gamma was determined by running the code with several different values and plotting the total number of fitted flares in all sources, the mean of the number of flares, and the number of fitted flares of 1ES 1959+650

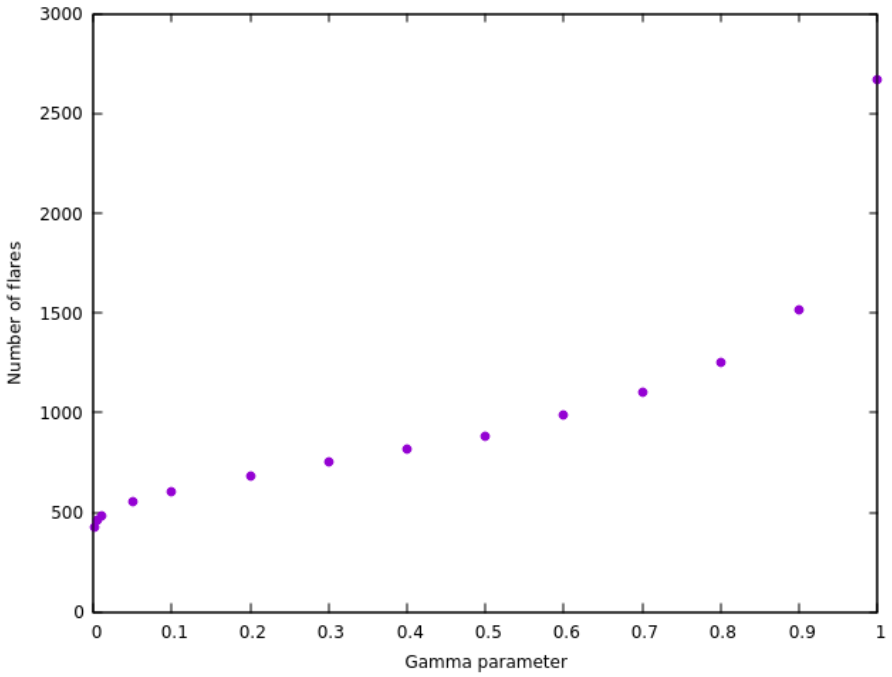

Figure 5. The plot of the total number of flares of all the sources against the gamma parameter, used to determine the appropriate value for the gamma parameter for fitting the data. In this graph, the values where the number of flares remained the most similar was where gamma was between 0.2-0.4.

against the gamma parameter. An example can be seen in Figure 5, which shows the total number of fitted flares in all sources against the gamma parameter. The optimal range for the gamma parameter was estimated to be around 0.2 - 0.5 where the curve is the flattest and the number of flares fitted therefore closer to constant. In order for the code to select only the largest flares, the smaller value of 0.2 was used in the fitting.

As an output, the Bayesian blocks code produces figures for the fits. Figures 6 and 7 show two examples of the fit where the flux density in Janskys is in y-axis and time in (Julian) days is in x-axis. In figure 6, the fit for the season 10 of RGB 1136+676 shows that the Bayesian block method detected slight variations in the flux density but this was not determined as a clear flare by the hill-climbing algorithm, and therefore it has no found flares. In Figure 7, the fit for the season

5 of BL Lac shows fast and significant variations in flux density, each found flare separated by a different colour. The computed statistics from the fits are output into two separate files. The first file has the information about the fitted blocks; their positions, flux densities, and uncertainties. The second file has the information about the flares identified by the hill-climbing algorithm; the flare peak times, peak flux densities, starting and ending times of the flares, and the uncertainties for all these produced parameters. Here flare peak is defined as the local maximum of the blocks in one flare, and the peak flux density is the flux density measured at the peak of the flare. Starting time and ending time of the flare are defined as those points in time where the hill-climbing algorithm has detected a change in the slope of the flux density from negative to positive in the case of starting time, and opposite for the ending time. In Figure 7, different colours signify each detected flare, and the starting and ending time are the start and end of each of these flares.

Since the exponential fitting tried previously is an unphysical model simply used to compute the duration, skewness, and flux density of the flares, the Bayesian blocks code is able to do the same without a priori knowledge about the shape of the flares. For the data used in this thesis, the Bayesian blocks method proved to be a better option to acquire the needed parameters. Because the data are not continuous, it is also better to not make many assumptions about what is happening in the jet between the data points. The Bayesian blocks code had also an option to tweak the time between the seasons to fit the whole light curve with the seasonal gaps but for clarity of the figures, the seasons were fitted separately so that one figure shows only the fit for one season.

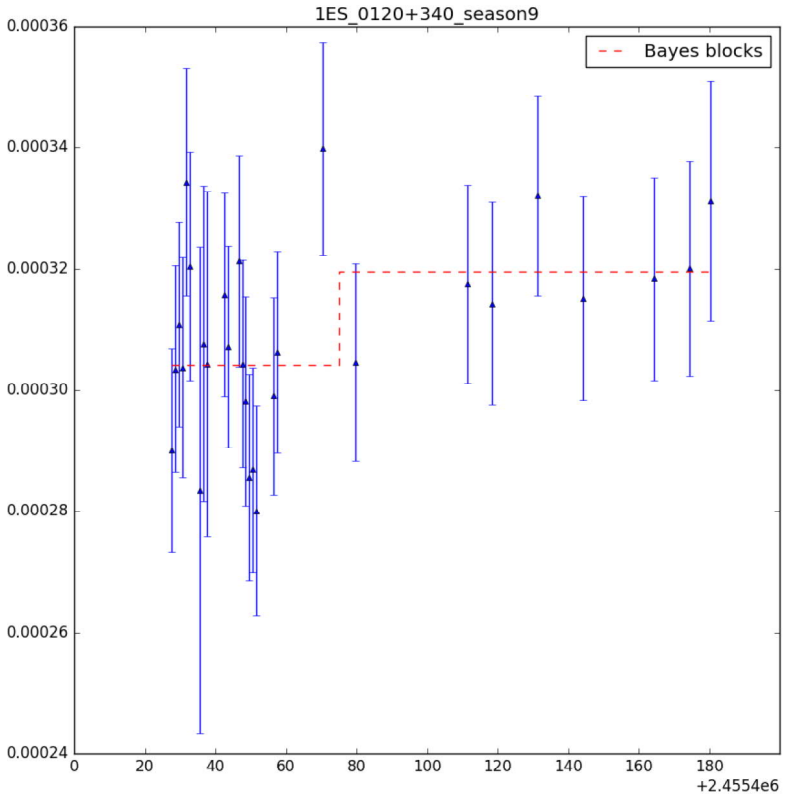

Figure 6. An example fit for season 10 of RGB 1136+676, for which the hill-climbing algorithm detected no clear flares. The y-axis is in Janskys and the x-axis is in Julian days starting from 22/07/2010. The gamma parameter used in the final fit was 0.2.

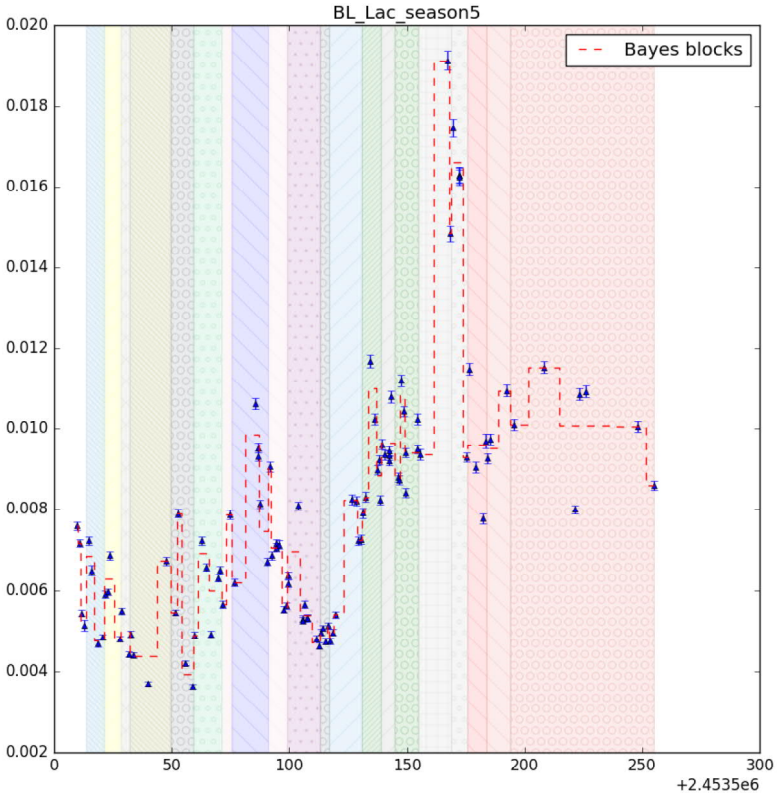

Figure 7. An example fit for season 5 of BL Lacertae, in which there can be seen a lot of noticeable variations in the flux density and multiple flares separated by different colours. The y-axis is in Janskys and the x-axis is in Julian days starting from 09/05/2005, and the gamma parameter used here again was 0.2.

3 Analysis

The parameters for each flare acquired from the fits were combined for all the different seasons of every target, and plotted using Python 2.7. Statistics of the sources were collected to Table 2 showing the number of data points, the number of seasons each dataset was divided into, the number of the flares given by the fits, and the median skewness of the flares ξ. The sources with zero or only one flare were not used in the analysis for their insufficient data. These include 1ES 0120+340, RGB 1417+257, and 1ES 1544+820.

Since the main focus of this thesis is to study the symmetry of the optical flares, the skewness of the flares was first computed in two different ways. The first skewness parameter simply compares the rise and decay times of the flares with the simple relation:

$$\text{skewness} = \frac{T_d}{T_r}, \tag{9}$$

where T_d is the decay time calculated from the subtraction of the flare peak time from the ending time, and T_r is the rise time of the flare, flare starting time subtracted from the peak time. Here, perfect symmetry naturally equals 1. Another way to examine the skewness of the flares was presented in [89], and later used in [69], where the skewness ξ was defined in the following way

$$\xi = \frac{T_d - T_r}{T_d + T_r}. \tag{10}$$

Here, perfect symmetry equals 0. If the rise time is slower than the decay time, the skewness is negative, and it is positive in the opposite case. Figures 8 and 9 show both skewness definitions for all the flares in BL Lacertae plotted as histograms

Table 2. Statistics of each source showing the number of the datapoints, the number of the seasons the lightcurves were divided into, the number of flares acquired from the fitting, and the median skewness ξ as defined in Equation 10

Target	Datapoints	Seasons	Flares	Median ξ
1ES 0033+595	387	11	12	0.6
1ES 0120+340	300	11	0	-
RGB 0136+391	393	11	14	0
RGB 0214+517	309	10	5	0.7
3C 66A	644	10	58	0
1ES 0647+250	303	10	9	0.2
1ES 0806+524	328	10	11	−0.1
OJ 287	699	10	70	0.1
1ES 1011+496	426	10	23	0.5
1ES 1028+511	273	10	2	0.7
Mkn 421	683	10	49	0
RGB 1117+202	230	10	8	−0.2
Mkn 180	378	10	17	0.1
RGB 1136+676	244	10	2	0
ON 325	271	10	21	0.1
1ES 1218+304	266	10	11	−0.2
RGB 1417+257	246	10	1	-
1ES 1426+428	219	10	4	0.2
1ES 1544+820	46	13	0	-
Mkn 501	749	11	17	0.1
OT 546	401	10	13	0.1
1ES 1959+650	734	11	34	0.1
BL Lac	771	12	108	0
1ES 2344+514	451	12	12	0
S5 0716+714	511	9	71	0.1
ON 231	195	7	19	0.2
3C 279	316	9	21	0.2
PG 1424+240	141	7	8	−0.1
PKS 1510-089	272	6	25	0
PG 1553+113	444	8	20	0.1
PKS 2155−304	109	11	16	−0.1

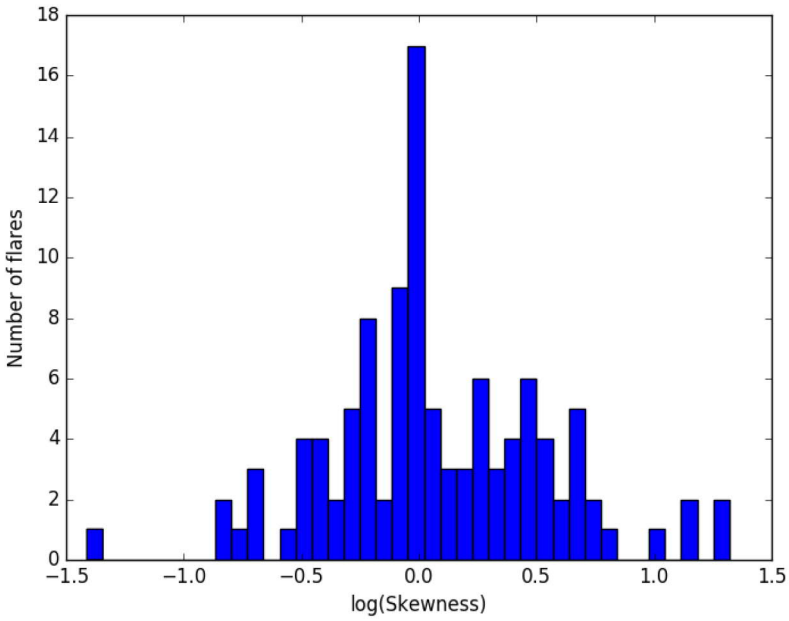

Figure 8. The skewness distribution in the logarithmic scale of the flares of BL Lacertae shows that the flares are predominantly symmetric but there still exists asymmetry on both sides even within one source.

against the number of the flares. From these figures and the statistical tests it was noticed that the two parameters represent the skewness in a similar way. Therefore in the future, only the results for the latter skewness ξ are shown for easier comparison with the results in [69, 73].

In addition to the skewnesses, luminosities of the flares were calculated as well as the redshift and Doppler corrected values for the luminosity, rise time, and duration of the flares. Knowing that the luminosity is related to the flux in the following way

$$L(\nu) = 4\pi d_L^2 S(\nu). \tag{11}$$

Lorentz transformation for intensity is $I_o(\nu_o) = D_{var}^3 I_i(\nu_i)$, where $I_o(\nu_o)$ is the observed intensity and $I_i(\nu_i)$ is the intrinsic intensity. Then the flux density is given

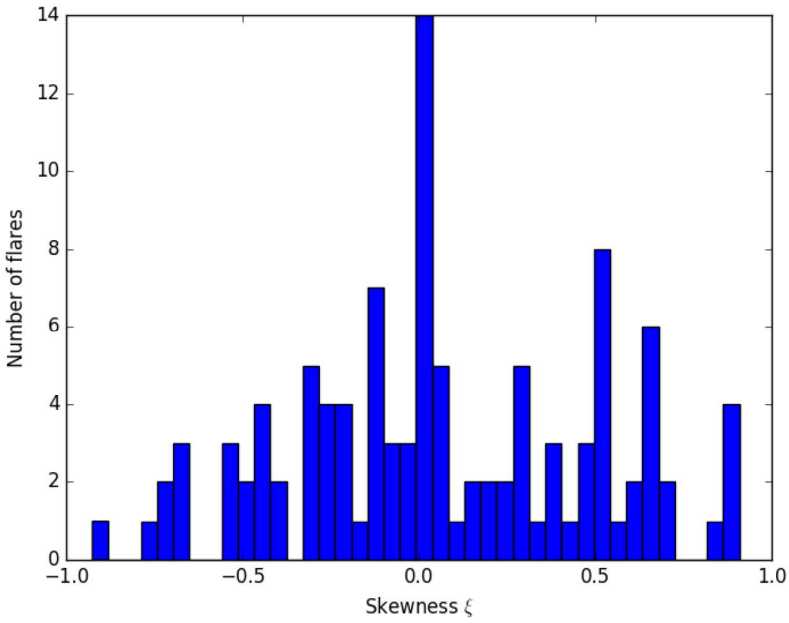

Figure 9. The skewness ξ (as in Chatterjee et al. 2012) of the flares of BL Lacertae. The results acquired with the two definitions of symmetry were considered to be similar hence only the results with ξ are shown.

by

$$S_o(\nu_o) = D_{var}^{3+\alpha} S_i(\nu_i). \tag{12}$$

Source at redshift z has a frequency $\nu_o = \dfrac{D_{var}\nu_i}{1+z}$. It then follows from Equations 11 and 12

$$t_i = \Big(\frac{D_{var}}{1+z}\Big) t_o \tag{13}$$

$$L_i = \Big(\frac{1+z}{D_{var}}\Big)^{3+\alpha} \frac{4\pi d_L^2}{1+z} S_o. \tag{14}$$

Here, t_o is the observed variability time, and t_i and L_i are the intrinsic values

of variability time and luminosity [90]. The redshifts and the variability Doppler factors are listed in Table 1. The corrections were done only for the sources with determined redshifts. The targets with missing variability Doppler factors but an existing redshifts were assumed to have a Doppler factor of 1 since they all are high peaking objects with usually less prominent Doppler boosting in the radio band [91]. Three objects, 1ES 1011+496, Mkn 501, and OT 546, had a Doppler factor less than one, which would refer to their jets being deboosted, and in their case it is more likely that their intrinsic brightness temperature $T_{b,int}$ is not the normally assumed equipartition temperature T_{eq}. Therefore, their determined Doppler factors are most likely not correct, and they were also assumed to have a Doppler factor of 1. It should be taken into account that the variability Doppler factors used here have been determined in the radio band and thus are possibly different than if these were determined in the optical band. The luminosity distances were calculated using the Cosmology Calculator [77]. For HBLs, the optical spectral index used here was $\alpha = -1.1$, and for LBLs and FSRQs $\alpha = -1.5$ [92]. A value of $\alpha = -1.3$ was used for IBLs [93].

The following sections describe the statistical analyses performed for these data, and the results acquired from these tests. Physical relevance of the results is then discussed in Section 4.

3.1 Statistical methods

The results from the fitting were analysed using the scipy.stats library for Python. The different parameters were tested by checking their correlation with each other to see if they have any effect on each other. Based on scatter plots created from the fits, some predictions could already be made to judge the reliability of the results.

The selected correlation test used in this thesis was Kendall's Tau-b because it is better for small sample size data than the Spearman rank-order correlation test.

The first assumption that needs to be fulfilled before analysing the data with the Kendall's Tau-b test is that the data have been measured on an ordinal or continuous scale, which the flux density data fulfils. The other one is that there is some monotonic relationship between the two parameters, but whereas the Spearman test explicitly requires this assumption to be fulfilled, the Kendall's Tau-b test is not as strict in this matter. The monotonicity of the parameters were checked by eye from the scatter plots created for the test. Because the monotonic relationship was not absolutely required in the Kendall's Tau-b test, the relationships with no visible monotonicity were tested nevertheless.

In the case of the redshift and Doppler corrected rise time, duration, and luminosity of the flares, additional partial correlation tests were ran for the pairs corrected rise time versus corrected luminosity, and corrected duration versus corrected luminosity. Since the corrected parameters have a relation according to Equations 13 and 14, it is necessary to see whether the detected correlation by Kendall's Tau-b test actually holds true by trying to find the unique variance between the tested parameters while eliminating the effects of the variables they are dependent on. Here the tested variables are corrected luminosity and the corrected rise time and corrected duration, and the control parameters are the Doppler factor and the redshift.

In addition, the 2-sample Kolmogorov-Smirnov test was done for the skewness histograms of the different blazar types to see whether they come from the same population or not.

3.2 Results

The results from the Kendall's Tau-b correlation tests are shown in Table 3. The table shows the tested parameter pairs, their correlation coefficients, their two-tailed significance (p-value), and the sample size. The correlation tests verified the visible connections that could already be expected from the scatter plots that were drawn

before the tests. In Table 3 the parameters that had a significant correlation at the 3σ level are marked with one asterisk (*) and the parameters with a significant correlation at the 2σ level are marked with two asterisks (**). It is important to notice that the sample size is not the same in all the tests. In the case of the corrected values, some of the sources did not have a defined redshift and therefore their corrected values could not be calculated. In the tests comparing the synchrotron frequency peak, the variability Doppler factor, and the Lorentz factor with the other parameters, the average and median values for each source were used, but only the median values are shown in the results as median is less prone to create bias. Again, some of the sources were missing the Doppler or Lorentz factors, making the sample size smaller than the overall number of the sources. The sample sizes should be taken into account when considering the significance of the correlation.

Table 4 shows the results of the partial correlation tests performed for the corrected values of rise time versus luminosity, and duration versus luminosity. The results show that no real correlation can be detected between the two parameters and that the correlation detected in the Kendall's Tau-b test follows simply from the definition of the corrections as seen in Equations 13 and 14.

The results for the K-S test can be seen in Table 5, which shows the tested pairs of blazar types, and the values for the K-S statistic, and the p-value. Here, results verified that the skewness histograms stem from the same population, which was already expected from the histograms in Figure 10.

Table 3. All the tested parameters, their correlation coefficients, (two-tailed) significances, and sample sizes. Correlation at the 3σ level is shown with * and correlation at the 2σ level is shown with **.

Tested parameters	Correlation	Significance	N
rise time vs. skewness*	−0.341	2.379e−40	680
flux density vs. skewness	−0.041	0.108	680
duration vs. skewness	0.037	0.148	680
corrected luminosity vs. skewness	−0.025	0.364	599
corrected rise time vs. skewness*	−0.272	2.617e−23	599
corrected duration vs. skewness	0.044	0.111	599
rise time vs. flux density*	−0.137	8.316e−8	680
rise time vs. luminosity	−0.010	0.711	599
duration vs. flux density*	−0.202	3.087e−15	680
corrected rise time vs. corrected luminosity*	−0.215	3.667e−15	599
corrected duration vs. corrected luminosity*	−0.248	9.427e−20	599
log[ν_{peak}] vs. # of flares (normalized by seasons)*	−0.450	0.001	28
log[ν_{peak}] vs. # of flares (normalised by data points)*	−0.523	9.323e−5	28
log[ν_{peak}] vs. median flux density	−0.252	0.060	28
log[ν_{peak}] vs. median rise time**	0.316	0.019	28
log[ν_{peak}] vs. median skewness	0.056	0.678	28
D_{var} vs. median flux density	0.213	0.269	15
D_{var} vs. median rise time*	−0.638	0.001	15
D_{var} vs. median skewness	−0.232	0.228	15
Γ vs. median flux density	−0.164	0.484	11
Γ vs. median rise time	−0.455	0.052	11
Γ vs. median skewness	0.200	0.392	11

Table 4. Results from the partial correlation tests done for corrected rise time, duration, and luminosity. The control parameters were variability Doppler factor and redshift. The results show that no actual correlation can be detected between these parameters when the effect of the controlling parameters is removed.

Tested pairs	Correlation	p-value
rise time vs. luminosity	−0.026	0.522
duration vs. luminosity	−0.041	0.314

Table 5. Results from the K-S test for differences in the skewness distributions of the different blazar populations.

Tested pairs	K-S statistic	p-value
HBL, IBL	0.070	0.654
HBL, LBL	0.069	0.667
HBL, FSRQ	0.109	0.715
IBL, LBL	0.071	0.754
IBL, FSRQ	0.141	0.433
LBL, FSRQ	0.118	0.662

4 Discussion

The main focus of this thesis is studying the symmetry of the blazar flares and how other time variability properties determined from the light curves can help explain the physics of the jet. The different measures of time variability, i.e. duration of the flare, the rise time, the decay time, and the ratio of the two; symmetry, are essential in the study of blazars for their extreme variability. There have been several studies of time variability in different wavelengths (e.g. in optical [3, 71], in radio [79, 80], and gamma-rays [94, 95]), but the symmetry of the flares in the optical to near-infrared wavelengths has not been studied extensively apart from a few sources (e.g. [69, 73]). In radio, [79] first introduced the exponential decomposition of the light curves, and the method used in this thesis is similar in principle. Several other studies of time variability have followed, utilizing the same or a similar tool to study the time variability properties, including symmetry, of blazars [69, 73, 80]. In their studies, [69, 73] have done comparisons of the gamma-ray and optical/NIR light curves, and studied the time variability properties of 6 and 10 blazars. This thesis has the advantage of a larger sample of 31 blazars consisting of all four different blazar types, and much longer time series.

4.1 Skewness

The symmetry of the flares was first examined by looking at how the skewness is distributed between the different blazar classes. Figure 10 shows the skewness distribution for each blazar type, and it can be confirmed that the flares in general are quite evenly distributed around the perfect symmetry, most flares being symmetric, but there also exists divergence to both sides of symmetry, negative and positive. Kolmogorov-Smirnov tests (Table 5) also confirm that the skewnesses of the different blazar types stem from the same population with each tested pair having a large p-value and therefore the distributions are expected to look similar. The symmetry is consistent with that determined by [69] where they compared the time variability of the gamma-ray and NIR flares and found the largest flares to be mostly symmetric in both wavelengths. The same was reported by [73]. In [69], the skewness of the optical long-term flares varied between the -0.5 to 0.5 and in [73] between -1.0 to 1.0, which are similar values as in Figure 10. Both studies suggest that the optical-IR symmetry of the flares could indicate that the long-term ($\sim$weeks to months) variability could be due to the light crossing time across the emission region. In their paper, [73] also studied the short-term flares of gamma-rays with durations of $\sim$hours but in optical wavelengths the cadence of days is the lower limit for the time bins. Therefore, the study of shortest optical flares is out of the reach of this thesis.

In order to test the differences between the exponential fitting used in [73] and the Bayesian blocks method used in this thesis, the data from [73] was examined by comparing the skewness distributions with the Kolmogorov-Smirnov test. The sources that were included in their paper and in this thesis were 3C 279, PKS 1510$-$089, PKS 2155$-$304, and OJ 187. Table 6 shows the results for the K-S test done for the skewness distributions derived from the exponential fits and from the Bayesian blocks fits of each pair. The p-values are large and the distributions can be assumed to stem from the same population. Therefore, the results acquired by

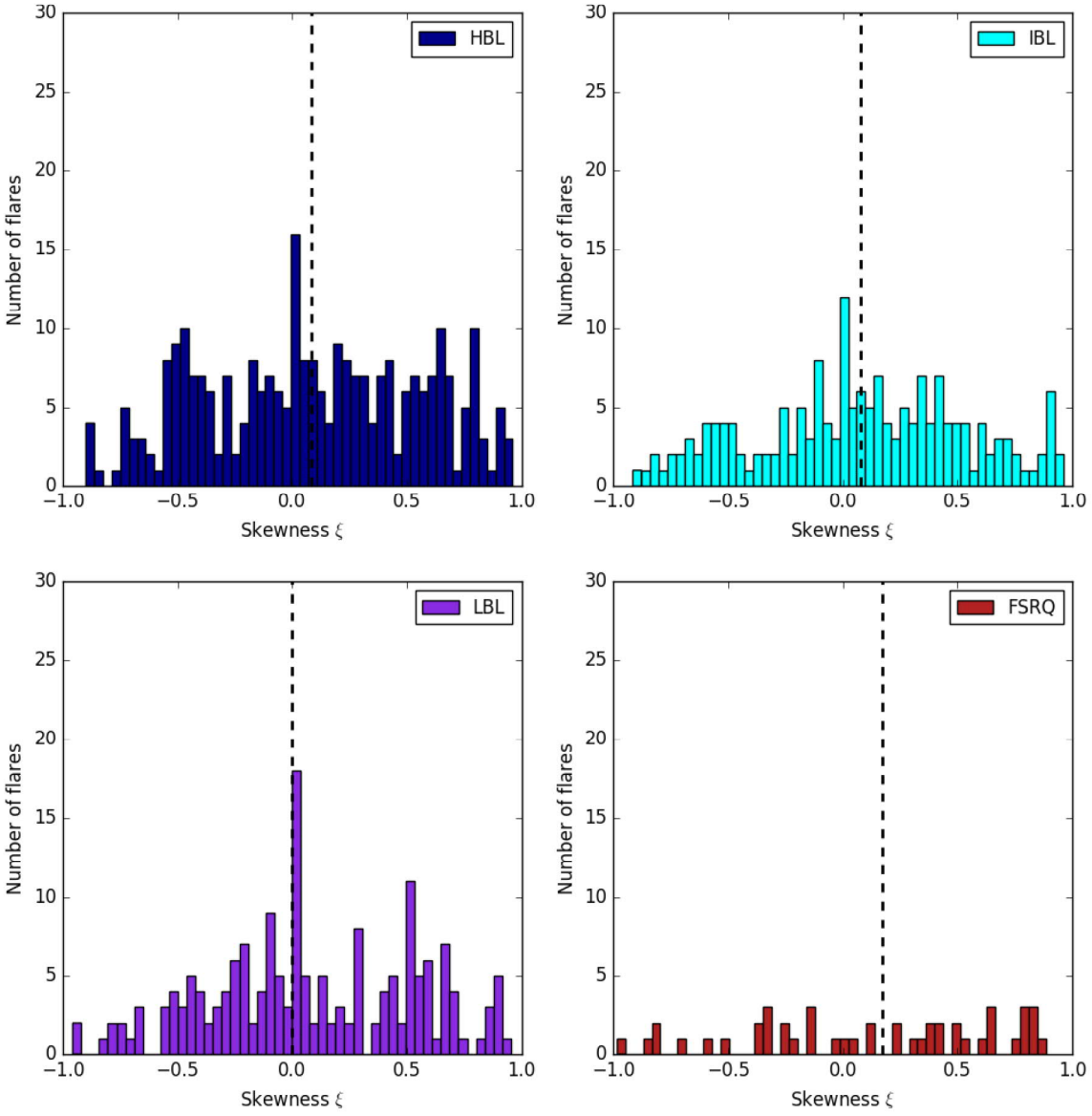

Figure 10. Skewness ξ distributions of the different blazar types. The dashed line shows the median of the distribution. K-S test showed that the different blazar types stem from the same population and the distributions are expected to look similar.

Table 6. K-S test between the skewnesses acquired by exponential fitting [73] and by Bayesian blocks fitting done in this thesis. Large p-values show that the results of Bayesian blocks fitting are comparable with the exponential fitting.

Tested source	K-S statistic	p-value
OJ 287	0.157	0.883
3C 279	0.179	0.819
PKS 1510-089	0.28	0.237
PKS 2155-304	0.25	0.719

the Bayesian blocks fitting are comparable to the results from exponential fitting. However, it should be noticed again that the sample sizes between this thesis and [73] are different; whereas this thesis used all the detected flares from all the observing seasons, [73] had only included one observing season in their study.

In order to relate the observed symmetry properties to the actual physics of the jet emission, [73] compared their observational results with the MUlti-ZOne Radiation Feedback (MUZORF) model by [96], which simulates the spectral variability patterns of a blazar using the internal shock model as its theoretical basis. In this model, two shells of plasma with different masses and internal energies travel at different speeds and collide. Their collision then forms forward and reverse shocks within the jet. The shocks propagate through the jet and instantaneously accelerate particles that will be seen as emission via different radiation mechanisms. The model was tested by changing the different parameters regarding the emission region in multiple runs. The rise and decay times of the flares were discussed to be possibly affected by the geometry of the emission region or due to particle acceleration and particle cooling [73, 97]. They found that the emission in all bands were dominated by the presence of shocks in the jet, optical emission by synchrotron radiation, X-ray emission by the SSC, and the higher energy emission by EC. They also found that the flares with faster rise than decay time (positively symmetric) could be caused by the larger or smaller base value of the bulk Lorentz factor, or broader or narrower inner or outer colliding plasma shells. Negatively symmetric flares were

possible when the outer shell was moving at a higher velocity than the inner shell so that the emission region was growing in size making particle acceleration more gradual. Changing the other parameters did not produce strong asymmetries in any waveband in the simulations.

In [55], the kink instability model for magnetic reconnection accelerating the particles in the jet was considered. Their model produced generally time-symmetric light curves and polarization signatures. This was thought to follow from the kink evolution time scale being comparable to the light crossing time scale, in which case asymmetric features disappear due to the light travel-time effects (LTTEs). They noticed that the symmetric features are produced in a moderately magnetized environment where the kink evolution time scale is governed by relativistic Alfvén speed, but in lower magnetization the Alfvén speed is non-relativistic and the radiation signatures become asymmetric with slower decay time. This could possibly explain the some asymmetric flares with longer decay times.

In this thesis, symmetry was also studied by looking for correlations with any of the other parameters derived from the fits. Table 3 shows the test results, some of which could already be expected from the scatter plots. Figure 11 shows the skewness against the rise times, durations, and Doppler and redshift corrected rise times and durations. Skewness has a significant negative correlation at the 3σ level with the rise time as well as the corrected rise time, which is expected from the definition of the skewness (Eq. 7). This is visualised in panels A and B of Figure 11 with the non-corrected and corrected rise time. We can see that the flares with longest durations tend to have a negative skewness meaning that their rise time is shorter than the decay time. Positively asymmetric flares have shorter rise times, but the flares with shorter rise times are scattered quite evenly on both sides of the skewness, positive skewness meaning their rise time is faster than the decay time. Correlation between the skewness and duration was not seen, which means that the

symmetry of the flares does not depend on its duration.

Figure 12 shows the skewness against the flux density, luminosity, and the Doppler and redshift corrected luminosity. None of these were found to correlate with the skewness indicating that the overall power of the outburst does not have an effect on the symmetry of the flares. The higher and lower power and luminosity flares seem to be evenly distributed on both sides of perfect symmetry. The peculiar zero symmetry flares seen in Figures 11 and 12 result from fast variations in the data with only few data points where the algorithm has created only a single block to describe the flare, thus its symmetry being exactly zero.

4.2 Comparing the blazar types

In addition to studying the symmetry, different features between the blazar types were analysed. A significant correlation was found between the number of the flares, both normalized by the number of seasons and the number of data points, and the synchrotron frequency peak (Figure 13). It appears that FSRQs produce more flares than BLLs in the same time frame based on the correlation found here. It was reported by [93,98] that FSRQs were found to produce higher amplitude variations than BLLs therefore being more variable. They also reported that LBLs were found to be more variable in amplitude than HBLs, IBLs being in between the two classes. However, here we see that the IBLs and LBLs appear to have more flares compared to the FSRQs, but FSRQs still having more flares than the HBLs, although this could be an effect of bias in the sample sizes of the blazar classes as there are only two FSRQs in our sample. In their paper, [93] explained the differences with LBLs and HBLs that LBLs are observed near their electron energy peak and in HBLs the emission originates from lower energy electrons. This is due to the fixed R-band, which detects electrons with different energies in sources with different SED peaks. Whereas the R-band in HBLs detects electrons at energies below those producing

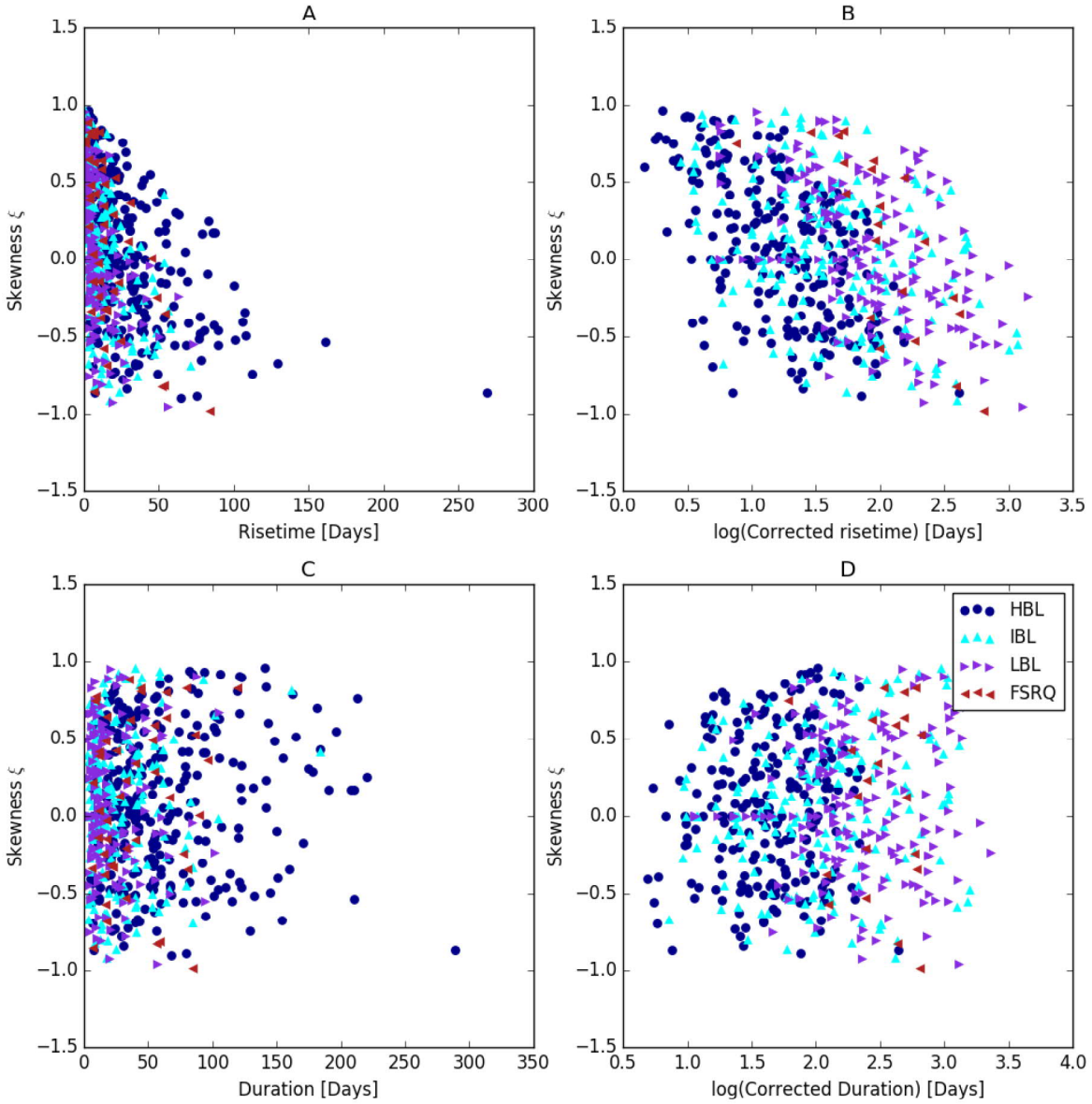

Figure 11. Skewness ξ plotted against the non-corrected rise times and durations as well as the Doppler and redshift corrected rise times and durations on logarithmic scale.

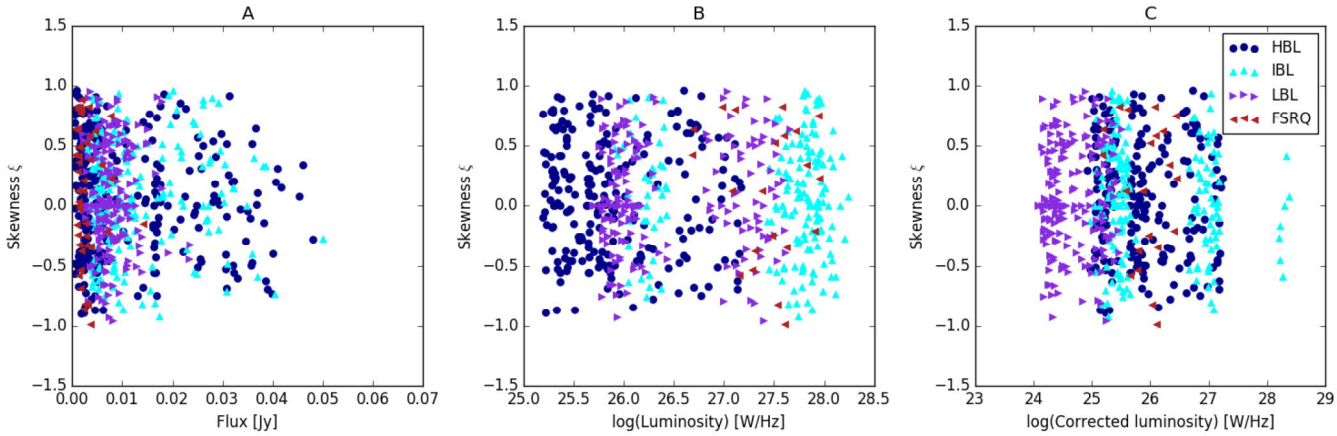

Figure 12. Skewness ξ plotted against the non-corrected flux density, luminosity, and the Doppler and redshift corrected luminosity.

the SED peak, in LBLs and FSRQs the R-band is near their peak frequency making these sources more variable. The differences between FSRQs and BLLs were thought to be due to the more efficient accretion in FSRQs, which shifts their SED peak to lower energies. Studying the differences between these classes might help uncover the underlying parent populations of the two source classes and be an important step in the unification of the AGN zoo. Similarities between LBLs and FSRQs, which can also be detected here in the number of flares, were justified by a suggestion in [19, 99] that the two classes are intrinsically similar but in LBLs the stronger jet emission hides the thermal emission usually detected in FSRQs.

Figure 14 shows the medians of skewness, rise time, and flux against the synchrotron frequency peak. No correlations were found between the flux or the skewness and the SED peak. The correlation that can be seen between the rise time and the synchrotron frequency peak follows from the Doppler boosting effects where the higher Doppler boosting shortens the rise times [100].

Despite there being only a few correlations between the other derived parameters, important remarks can be made by looking at how the different blazar types are positioned compared to each other. Figure 15 shows comparisons of flux density,

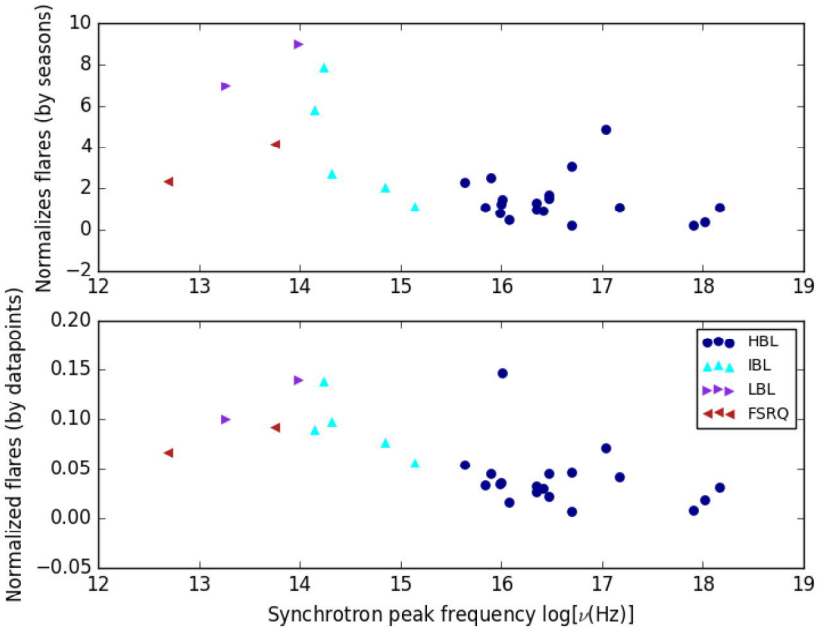

Figure 13. Scatter plot of the number of flares normalized by the number of season and the number of flares normalized by the number of datapoints against the synchrotron frequency peak. This shows that HBLs appear to have less flares compared to IBLs, LBLs, and FSRQs.

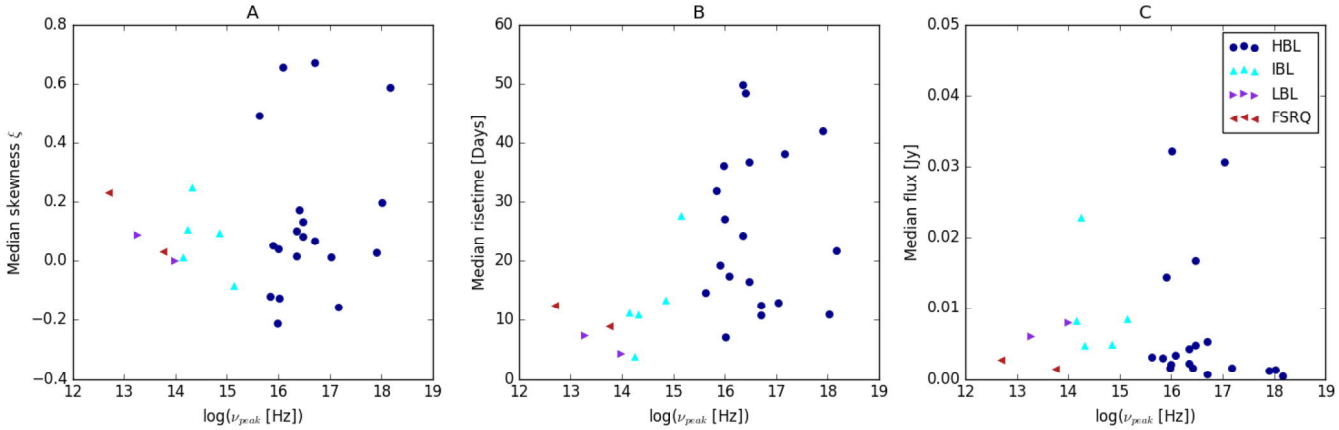

Figure 14. The median skewnesses ξ, rise times, and flux densities each source plotted against their synchrotron frequency peaks $\log(\nu_{peak}[\mathrm{Hz}])$

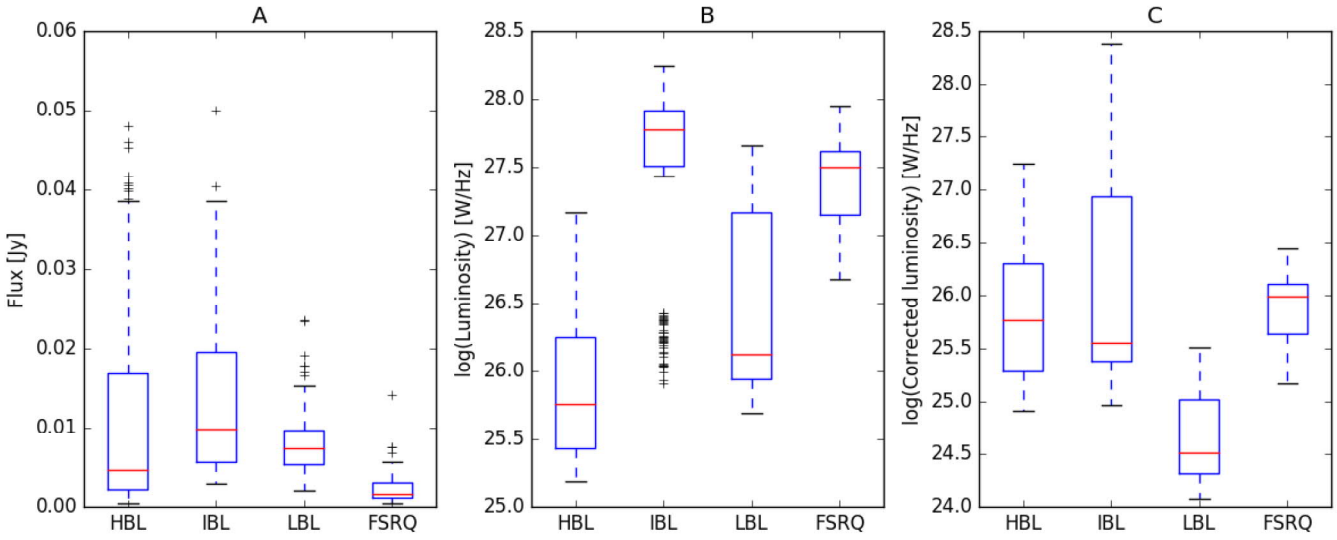

Figure 15. Boxplots of the non-corrected flux densities, luminosities, and the corrected luminosities for each blazar type. Here the boxes extend from the upper to the lower quartile of the data. The red line inside the box shows the median of the data, and the whiskers show the full range of data. Outliers are marked by crosses.

luminosity, and the corrected luminosity for each blazar type. In their papers, [93,98] reported that FSRQs seem to have higher amplitude variations compared to BL Lacs. In the sample used in this thesis, HBLs, IBLs, and LBLs tend to have higher flux densities than FSRQs, but the non-corrected luminosity is lower in HBLs than in the other three types of blazars. When corrected for the redshift and the Doppler boosting, HBLs and IBLs reach highest luminosities but it appears that despite HBLs producing higher amplitude flares, their median luminosity is still somewhat lower than in FSRQs, which is in accordance with [93, 98]. However, the larger sample size of HBLs compared to the rest of the types might cause a bias in the statistics and this might not truly represent the typical flux densities and luminosities detected from IBLs, LBLs, and FSRQs.

Another feature that could further support the intrinsic similarities of FSRQs and LBLs can be seen in Figure 16. The non-corrected rise times clearly show the effects of Doppler boosting on the lower peaking sources with their shorter rise times

and durations. In the corrected panels (B and D) the differences between the higher peaking sources and the lower peaking sources are further highlighted, showing that the rise times and durations of FSRQs and LBLs are actually longer compared to HBLs and IBLs.

4.3 Other correlations

The correlation tests showed that the skewness did not correlate with any other parameters derived from the fits. Correlations between the other parameters were also studied by Kendall's tau-b tests and by plotting them against each other in scatter plots. Figure 17 shows the flux density against the rise time, and corrected luminosity against the corrected rise time. From panel A, we can see that the highest flux flares are also the shorter ones whereas the longer flares tend to be in the lower power area. Non-corrected rise time and flux density were found to correlate significantly at the 3σ level as was the case with non-corrected duration and flux density.

Corrected values of rise time and luminosity, as well as corrected values of duration and luminosity, were found to correlate at the 3σ level, but because of their definition (Eqs. 14 and 13) both are dependent on the Doppler factor and the redshift, therefore, a partial correlation test was done in order to detect true correlation. Table 4 shows the results for corrected duration and rise time against the corrected luminosity. Both of these previously detected correlations disappear, and are purely caused by the Doppler beaming. This is in accordance with [101] where they noticed that in the radio regime the duration of the flare and the observed peak luminosity are not correlated. They found a weak correlation with the non-Doppler corrected peak flux density and the duration but the correlation disappeared with the corrected values. Thus, Doppler boosting is the cause for the detected correlation between the time, flux density, and luminosity parameters of the flares.

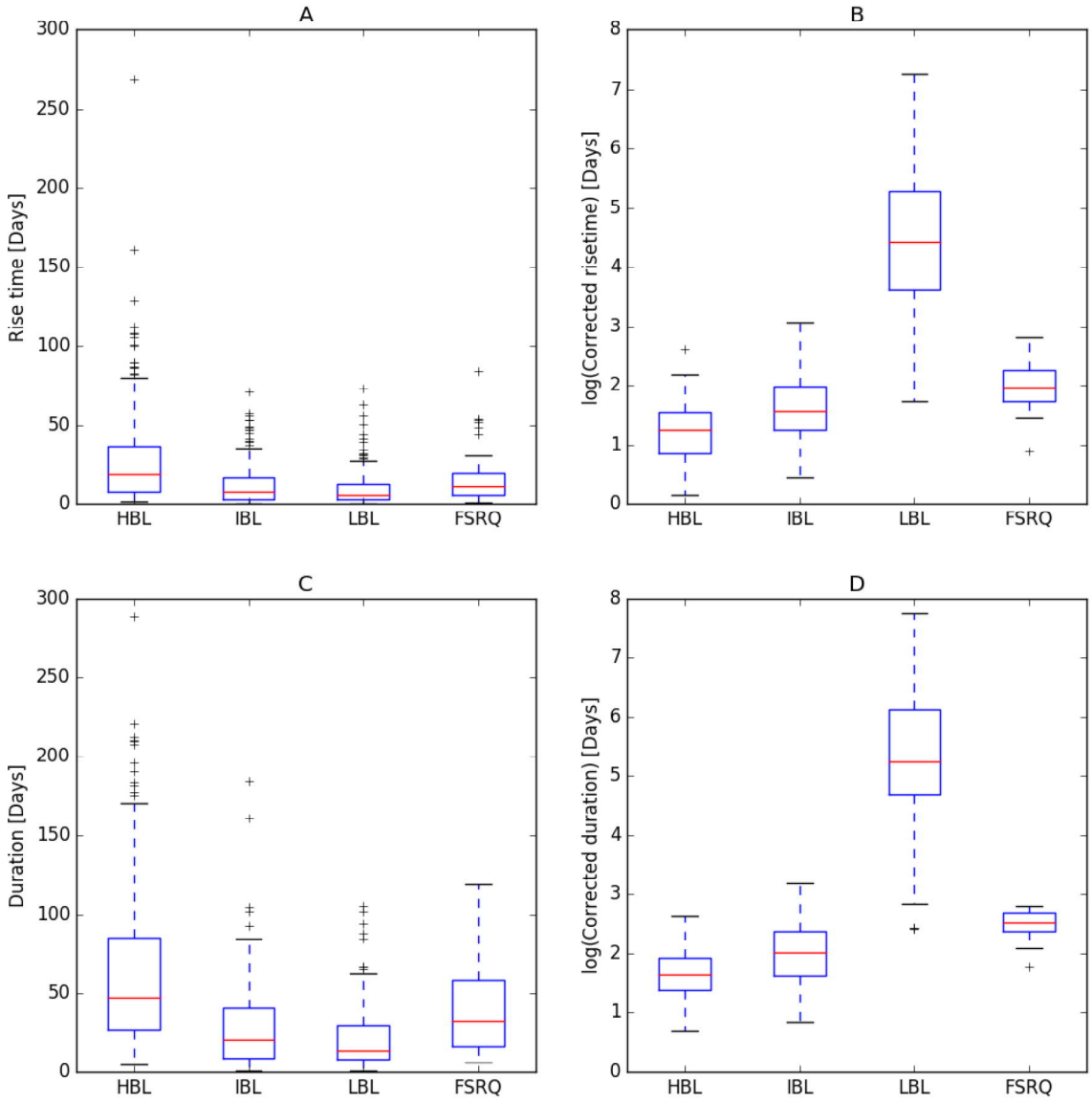

Figure 16. Boxplots of the non-corrected rise times and durations as well as the corrected rise times and durations on the logarithmic scale for each blazar type.

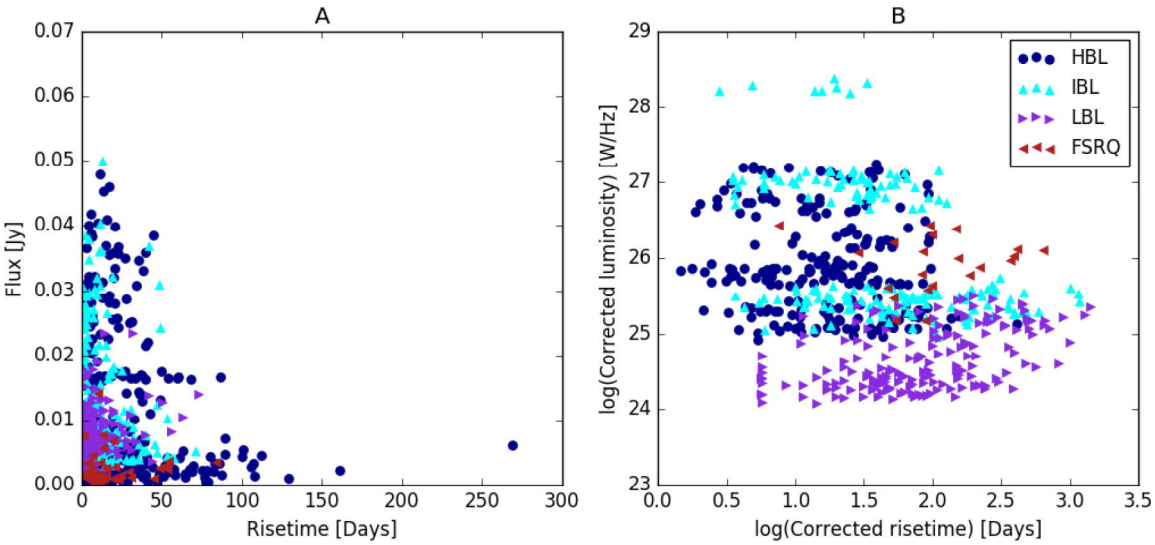

Figure 17. Plots of flux density against the rise time, and the corrected luminosity against the corrected rise time both on logarithmic scale.

Correlation between the medians of the derived parameters of each source and the variability Doppler factor and the bulk Lorentz factor were also studied. Figures 18 and 19 show the scatter plots of each tested pair. Only the rise time and the Doppler factor were found to correlate as expected due to the greater Doppler boosting foreshortening the observed time scales. The relationship between the Lorentz factor and rise time appears similar to this, but no correlation was found between the two. The rest of the parameters were not correlated, therefore, Doppler boosting does not affect the symmetry of the flares and its effect on flux density is not clear in this small sample of objects.

4.4 Future possibilities

Studying the time variability further in the future gives a means to constrain the sizes and the locations of the multiwavelength emission and how it is produced [69], and it might help in the study of the magnetic field of the jet [55, 64] There are several models trying to describe the acceleration of the particles in the blazar jets

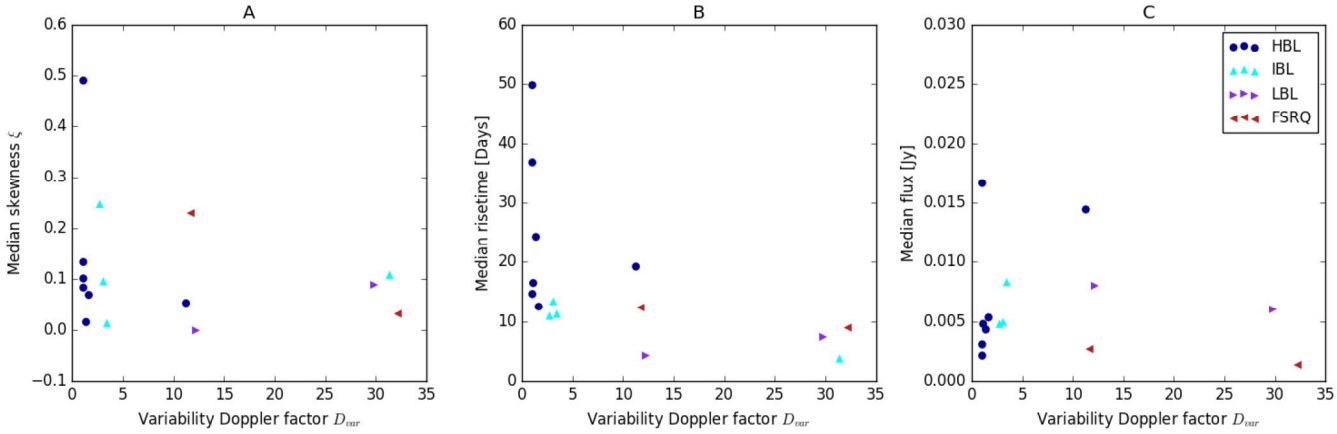

Figure 18. Median skewnesses ξ, rise times, and flux densities against the variability Doppler factors D_{var}.

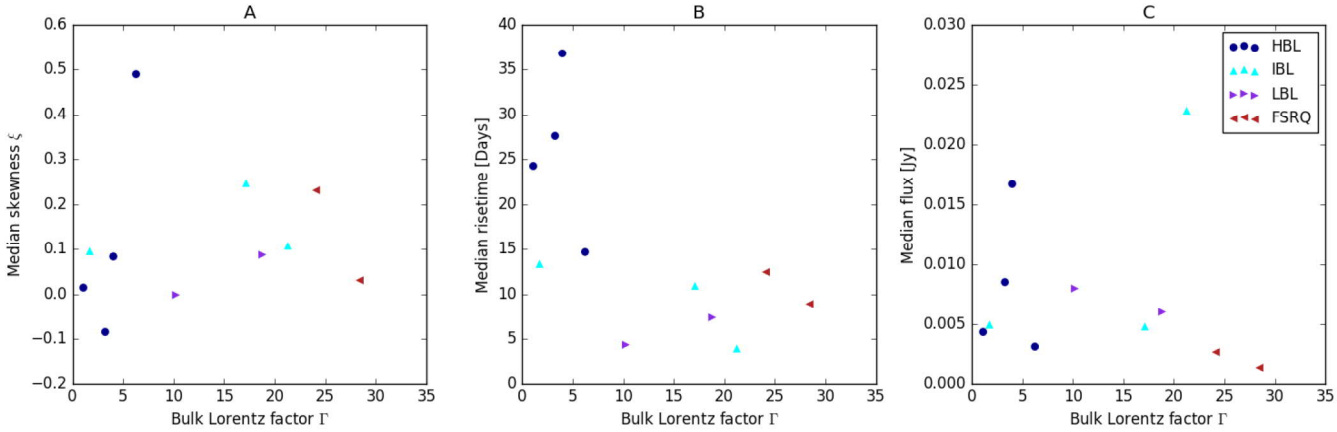

Figure 19. Median skewnesses ξ, rise times, and flux densities against the bulk Lorentz factors Γ

but multiwavelength and polarization observations of the variability are essential in uncovering the physics behind these phenomena.

As was already discussed in Section 4.1, multiwavelength time variability studies and studies of symmetry could help uncover the physics of the jet and properties of the emission region [73]. In their study, [69] found that the optical-IR and the gamma-ray variability were correlated and this could support the leptonic model where the same population of electrons causing the IR emission is also the source of the HE emission through synchrotron and IC processes. They also state that their observations do not exclude hadronic models, and further studies are needed. The correlation between the time variability at different frequencies could also be used to find out the lower limit of the magnetic field of the jet if the time delay between these frequencies is caused by the different radiative cooling time scales of the electrons at these energies [102].

By connecting the studies of the time variability in different wavelengths to the polarization studies, the magnetic field of the jet and therefore the possible acceleration mechanisms could be studied more closely. Magnetic fields could be an efficient way to accelerate the particles in the jet through magnetic reconnection [55] or shocks in an ordered magnetic field [103]. In their paper, [55] presented the kink instability model where the blazar emission zone could be highly magnetized, and the model was able to produce the polarization signatures similar to the observations that the previously assumed shock model has not been able to produce. Also the polarization time variability properties have been observed to be symmetric similarly to the flux density variations [104, 105]. Thus, including polarization information into the study could help to better constrain the different models.

5 Conclusions

In this thesis I studied the symmetry of the optical flares in blazar light curves. This was done by utilizing a Bayesian blocks method to divide the long-term light curves of each source into individual flares and by computing the symmetry and other parameters from the flare data. This study has the advantage of a larger sample size compared to other similar studies.

The main results considering the symmetry of the flares are that the symmetry of the flares was found to be evenly distributed on both sides of perfect symmetry in all four blazar types and that they stem from the same population. This is consistent with [69, 73]. They suggested that the optical-IR variability could be linked with the light crossing time across the emitting region in the jet. Negatively asymmetric flares were then thought to be produced when the acceleration of the particles was more gradual due to a growing emission region. On the other hand, [55] explained the symmetric features being produced in moderately magnetized environments, and the asymmetry being a result from the lower magnetization when the Alfvén speed is non-relativistic, creating positively asymmetric flares.

When comparing the blazar types, FSRQs were found to produce more flares compared to HBLs, and the similarities between the low-peaking sources in the number of flares were in accordance with [93] and [19, 99] who suggested that the two classes could be intrinsically similar but the stronger jet emission from LBLs drowns the thermal emission that is usually seen in FSRQs as the "blue bump". FSRQs and LBLs were found to be similar also in terms of the corrected time scales of the flares, although the small sample size of the lower peaking sources in this thesis does create some bias to the results.

Although this study found no unexpected behaviour or trends in the symmetry of the flares, this study was useful in a sense that it was the first systematic study using a large sample of objects with long-term light curves, and it supports earlier

findings from studies on individual sources.

References

[1] D. Lynden-Bell, Nature **223**, 690 (1969).

[2] N. I. Shakura and R. A. Sunyaev, A&A **24**, 335 (1973).

[3] R. Chatterjee *et al.*, ApJ **689**, 79 (2008).

[4] A. P. Marscher *et al.*, Nature **452**, 966 (2008).

[5] A. P. Marscher *et al.*, ApJ **710**, L126 (2010).

[6] S. G. Jorstad *et al.*, ApJ **715**, 362 (2010).

[7] M. L. Ahnen *et al.*, A&A **593**, A91 (2016).

[8] R. J. Britto *et al.*, ApJ **830**, 162 (2016).

[9] T. Hovatta *et al.*, A&A **912**, 899 (2007).

[10] J. H. Krolik, *Active Galactic Nuclei: From the Cetnral Black Hole to the Galactic Environment* (Princeton University Press , 1999), pp. 4–17.

[11] C. M. Urry and P. Padovani, PASP **107**, 803 (1995).

[12] J. H. Krolik, *Active Galactic Nuclei: From the Central Black Hole to the Galactic Environment* (Princeton University Press , 1999), pp. 424–427.

[13] S. S. Holt, S. G. Neff, and C. M. Urry, AIP Conference Proceedings **254**, (1992).

[14] M. Türler *et al.*, Astronomy and Astrophysics Supplement Series **134**, 89 (1999).

[15] M. Rowan-Robinson, ApJ **213**, 635 (1977).

[16] A. Lawrence and M. Elvis, ApJ **256**, 410 (1982).

[17] J. H. Krolik, *Active Galactic Nuclei: From the Central Black Hole to the Galactic Environment* (Princeton University Press , 1999), pp. 8–11.

[18] R. Scarpa and R. Falomo, A&A **325**, 109 (1997).

[19] P. Giommi, P. Padovani, and G. Polenta, MNRAS **431**, 1914 (2013).

[20] B. L. Fanaroff and J. M. Riley, MNRAS **167**, 31P (1974).

[21] H. Landt and H. E. Bignall, MNRAS **391**, 967 (2008).

[22] P. Kharb, M. L. Lister, and N. J. Cooper, ApJ **710**, 764 (2010).

[23] A. A. Abdo *et al.*, ApJ **716**, 30 (2010).

[24] M. Georganopoulos and A. P. Marscher, ApJ **506**, 621 (1998).

[25] R. C. Vermeulen, P. M. Ogle, H. D. Tran, and E. Al., ApJ **452**, (1995).

[26] E. A. Corbett, A. Robinson, D. J. Axon, and J. H. Hough, MNRAS **311**, 485 (2000).

[27] C. M. Raiteri, A&A **464**, 871 (2007).

[28] G. Fossati and E. T. Meyer, ASP Conference Series **427**, 141 (2010).

[29] K. Nilsson *et al.*, A&A **400**, 95 (2003).

[30] J. K. Kotilainen, R. Falomo, and R. Scarpa, A&A **332**, 503 (1998).

[31] R. A. Laing, J. V. Jenkins, J. V. Wall, and S. W. Unger, ASP Conference Series **54**, 201 (1994).

[32] D. S. De Young, ApJ **405**, L13 (1993).

[33] A. Tchekhovskoy and O. Bromberg, MNRAS **461**, L46 (2016).

[34] A. P. Marscher, ASP Conference Series **144**, 25 (1998).

[35] J. N. Bregman, M. J. Lebofsky, A. F. Margo, and E. Al., Nature **293**, 714 (1981).

[36] C. M. Urry and R. F. Mushotzky, ApJ **253**, 38 (1982).

[37] L. Maraschi, G. Ghisellini, and A. Celotti, ApJ **397**, L5 (1992).

[38] J. Chiang and M. Böttcher, ApJ **564**, 92 (2002).

[39] C. Arbeiter, M. Pohl, and R. Schlickeiser, ApJ **627**, 62 (2005).

[40] M. Sikora, M. C. Begelman, and M. J. Rees, ApJ **421**, 153 (1994).

[41] C. D. Dermer, J. D. Finke, H. Krug, and M. Böttcher, ApJ **692**, 32 (2009).

[42] K. Mannheim and P. L. Biermann, A&A **253**, (1992).

[43] A. Mücke and R. J. Protheroe, Astroparticle Physics **15**, 121 (2001).

[44] A. Mücke *et al.*, Astroparticle Physics **18**, 593 (2003).

[45] A. H. Bridle and R. A. Perley, ARAA **22**, 319 (1984).

[46] R. A. Laing, Nature **331**, 149 (1988).

[47] A. Lähteenmaki and E. Valtaoja, ApJ **521**, 493 (1999).

[48] M. L. Lister *et al.*, AJ **152**, 1 (2016).

[49] M. J. Rees, Nature **211**, 468 (1966).

[50] A. P. Marscher and W. K. Gear, ApJ **298**, 114 (1985).

[51] P. A. Hughes, H. D. Aller, and M. F. Aller, ApJ **298**, 301 (1985).

[52] M. Spada, G. Ghisellini, D. Lazzati, and A. Celotti, MNRAS **325**, 1559 (2001).

[53] M. Joshi and M. Bottcher, ApJ **662**, 884 (2007).

[54] P. B. Graff, M. Georganopoulos, E. S. Perlman, and D. Kazanas, ApJ **689**, 68 (2008).

[55] H. Zhang, H. Li, F. Guo, and G. Taylor, ApJ **835**, 125 (2017).

[56] J. G. Kirk and P. Duffy, Journal of Physics G: Nuclear and Particle Physics **25**, 1 (1999).

[57] R. Vainio, J. J. P. Virtanen, and R. Schlickeiser, A&A **409**, 821 (2003).

[58] J. J. P. Virtanen and R. Vainio, ApJ **621**, 313 (2005).

[59] E. Angelakis *et al.*, MNRAS **463**, 3365 (2016).

[60] D. Giannios and H. Spruit, A&A **450**, 887 (2006).

[61] L. Sironi, M. Petropoulou, and D. Giannios, MNRAS **450**, 183 (2015).

[62] Y. Mizuno, Y. Lyubarsky, K. I. Nishikawa, and P. E. Hardee, ApJ **700**, 684 (2009).

[63] X. Guan, H. Li, and S. Li, ApJ **781**, (2014).

[64] I. M. Christie, M. Petropoulou, L. Sironi, and D. Giannios, MNRAS **82**, 65 (2019).

[65] M. Petropoulou, D. Giannios, and L. Sironi, MNRAS **462**, 3325 (2016).

[66] C. Hoffmeister, Astronomische Nachrichten **236**, 233 (1929).

[67] P. A. Strittmatter, K. Serkowski, and R. Carswell, ApJ **175**, (1972).

[68] R. Falomo, E. Pian, and A. Treves, Astron Astrophys Rev **22**, 73 (2014).

[69] R. Chatterjee *et al.*, ApJ **749**, 191 (2011).

[70] J. R. P. Angel and H. S. Stockman, ARAA **18**, 321 (1980).

[71] K. Nilsson *et al.*, A&A **620**, A185 (2018).

[72] A. Sillanpää, S. Haarala, and M. J. Valtonen, ApJL **325**, 628 (1988).

[73] N. Roy, R. Chatterjee, J. Manasvita, and A. Ghosh, MNRAS **482**, 743 (2018).

[74] E. Takalo, L. O. Nilsson, K. Lindfors, AIP Conference Proceedings **Vol. 1085**, 705 (2008).

[75] K. Nilsson, *Diffphot v1.16 manual* (Tuorla Observatory & Finnish Center for Astronomy with ESO (FINCA) , 2015).

[76] L. Costamante and G. Ghisellini, A&A **384**, 56 (2002).

[77] E. L. Wright, PASP **118**, 1711 (2006).

[78] I. Liodakis *et al.*, ApJ **866**, 137 (2018).

[79] E. Valtaoja, A. Lahteenmaki, H. Terasranta, and M. Lainela, The Astrophysical Journal Supplement Series **120**, 95 (1999).

[80] T. Hovatta, E. Valtaoja, M. Tornikoski, and A. Lähteenmäki, A&A **494**, 527 (2009).

[81] J. Scargle, ApJ **504**, 405 (1998).

[82] J. D. Scargle, J. P. Norris, B. Jackson, and J. Chiang, ApJ **764**, 167 (2013).

[83] A. C. S. Readhead, ApJ **426**, 51 (1994).

[84] A. Lähteenmäki, E. Valtaoja, and K. Wiik, ApJ **511**, 112 (1999).

[85] M. Böttcher, D. E. Harris, and H. Krawczynski, *Relativistic Jets from Active Galactic Nuclei* (Wiley-VCH , 2012), pp. 32–38.

[86] T. Savolainen *et al.*, A&A **394**, 851 (2002).

[87] D. Huppenkothen *et al.*, ApJ **810**, 66 (2015).

[88] B. J. Brewer, L. B. Pártay, and G. Csányi, Stat Comput **21**, 649 (2011).

[89] A. A. Abdo *et al.*, ApJ **722**, 520 (2010).

[90] A. K. Kembhavi and J. V. Narlikar, *Quasars and Active Galactic Nuclei: An Introduction* (Cambridge: Cambridge Univ. Press , 1999), pp. 57–59.

[91] M. L. Lister *et al.*, ApJ **742**, 27 (2011).

[92] M. Fiorucci, S. Ciprini, and G. Tosti, A&A **419**, 25 (2004).

[93] T. Hovatta *et al.*, MNRAS **439**, 690 (2014).

[94] K. Nalewajko, MNRAS **430**, 1324 (2013).

[95] S. Saito *et al.*, ApJL **766**, 1 (2013).

[96] M. Joshi and M. Boettcher, ApJ **727**, 21 (2010).

[97] M. Sasada, S. Mineshige, S. Yamada, and H. Negoro, PASJ **69**, 1 (2017).

[98] A. Bauer *et al.*, ApJ **699**, 1732 (2009).

[99] P. Giommi *et al.*, MNRAS **420**, 2899 (2012).

[100] E. Nieppola *et al.*, A&A **488**, 867 (2008).

[101] T. Hovatta *et al.*, A&A **485**, 51 (2008).

[102] T. Takahashi *et al.*, ApJ **470**, L89 (1996).

[103] H. Zhang, W. Deng, H. Li, and M. Böttcher, ApJ **817**, 63 (2015).

[104] A. A. Abdo *et al.*, Nature **463**, 919 (2010).

[105] D. Blinov *et al.*, MNRAS **453**, 1669 (2015).